Chemico-Biological Interactions 406 (2025) 111318

Contents lists available at ScienceDirect

Chemico-Biological Interactions

journal homepage: www.elsevier.com/locate/chembioint

Research paper

The effect of a varying pyridine ligand on the anticancer activity of Diiron (I) bis-cyclopentadienyl complexes

Annachiara Rossi [a], Lorenzo Biancalana [a], Ján Vančo [b], Tomáš Malina [b,c], Stefano Zacchini [d], Zdeněk Dvořák [e], Zdeněk Trávníček [b,**], Fabio Marchetti [a,*]

[a] University of Pisa, Department of Chemistry and Industrial Chemistry, Via Giuseppe Moruzzi 13, I-56124, Pisa, Italy
[b] Regional Centre of Advanced Technologies and Materials, Czech Advanced Technology and Research Institute, Palacký University, Šlechtitelů 27, CZ-779 00, Olomouc, Czech Republic
[c] Nanotechnology Centre, Centre for Energy and Environmental Technologies, VŠB–Technical University of Ostrava, 17. listopadu 2172/15, CZ-708 00, Ostrava, Poruba, Czech Republic
[d] University of Bologna, Dipartimento di Chimica Industriale "Toso Montanari", Via Piero Gobetti 85, I-40129, Bologna, Italy
[e] Department of Cell Biology and Genetics, Faculty of Science, Palacký University, Šlechtitelů 27, CZ-779 00, Olomouc, Czech Republic

ARTICLE INFO

Keywords:
Bioorganometallic chemistry
Metals in medicine
Diiron complexes
Pyridine ligand
In vitro cytotoxicity
Cellular effects

ABSTRACT

The new diiron complexes $[Fe_2Cp_2(CO)(L)(\mu\text{-}CO)\{\mu\text{-}CN(Me)(Cy)\}]CF_3SO_3$ (L = pyridine, **3a**; 4-aminopyridine, **3b**; 4-dimethylaminopyridine, **3c**; 4-trifluoromethylpyridine, **3d**; nicotinic acid, **4**; Cp = η^5-C_5H_5, Cy = C_6H_{11} = cyclohexyl) were synthesized in moderate to high yields using two distinct synthetic routes from the precursors **1** (L = CO, for **4**) and **2** (L = NCMe, for **3a-d**), respectively. All products were characterized by IR and multinuclear NMR spectroscopy, and the structures of **3b** and **3d** were ascertained by X-ray diffraction studies. The behavior of the complexes in aqueous solutions (solubility, Log P_{ow}, stability) was assessed using NMR and UV–Vis methods. The *in vitro* antiproliferative activity of **3a-c** and **4** was evaluated against seven human cancer cell lines (A2780, A2780R, A549, MCF-7, PC3, HOS and HT-29) and one normal cell line (MRC-5), following 24 h of incubation (MTT test). Overall, **3**–**4** demonstrated stronger cytotoxicity than cisplatin, with **3c** emerging as the most potent compound. The activity seems primarily linked to the inhibition of metabolic processes in the cancer cells, including depletion of reactive oxygen species (ROS) levels. However, subtle differences have been observed between the complexes, with **4** exerting its cytotoxicity through a distinct multimodal mechanism.

1. Introduction

Transition metal complexes can play an important role in the development of new and efficient anticancer drugs, due to their peculiar properties including a wide availability of structures and geometries, a feasible redox chemistry centered on the metal, and the possible release of ligands [1–4]. Nowadays, a few platinum compounds are used worldwide in the hospital treatment of different types of tumours [5–7] but, despite their efficacy, they manifest some limitations arising from severe side effects and resistance phenomena [8–10]. To overcome these limitations, compounds based on other transition metals have been widely considered as alternatives [11–13], and, in this regard, endogenous metals may represent an advantageous choice to limit toxicity issues [14,15]. Specifically, organometallic monoiron(II) complexes containing one (piano-stool complexes) [16,17] or two cyclopentadienyl ligands (ferrocenes) [18–20] have emerged as promising anticancer agents. Several studies have been conducted in vivo, showing a range of inhibition effects [21–24] including the stimulation of tumor growth [25–27]. In general, the mode of action of these compounds relies on the production of reactive oxygen species (ROS) promoted by Fe^{II} to Fe^{III} intracellular oxidation [18,19]. Recently, we have unveiled the anticancer potential of dinuclear iron(I) complexes based on the $\{Fe_2Cp_2(CO)_x\}$ core (x = 2–3, Cp = η^5-C_5H_5). This dimetallic core enables cooperative effects resulting in greater synthetic opportunities [28–31], and particularly cationic aminocarbyne derivatives (FEA) can be easily obtained, even in multigram scales, through a straightforward synthetic route (Scheme 1A) [32,33]. FEA complexes are generally robust in physiological solutions, and their cytotoxicity is predominantly related

* Corresponding author.
** Corresponding author.
E-mail addresses: zdenek.travnicek@upol.cz (Z. Trávníček), fabio.marchetti@unipi.it (F. Marchetti).

https://doi.org/10.1016/j.cbi.2024.111318
Received 14 October 2024; Received in revised form 16 November 2024; Accepted 25 November 2024
Available online 26 November 2024

to the intracellular disaggregation of the diiron structure [34], leading to iron species being responsible for enhanced ROS production and inhibition of TrxR (thioredoxin reductase) [35,36]. A screening study highlighted the beneficial effect of incorporating the cyclohexyl group (Cy) for cytotoxicity and selectivity towards cancer cells [34]. Cyclohexyl has been regarded to facilitate the cellular uptake of different metal compounds, presumably due to its compact and hydrophobic structure [37–40].

The replacement of one CO ligand from **1** may lead to increased antitumor potential, and we recently disclosed that a specific derivative (FEACYP, Scheme 1B) combines an excellent water solubility with a strong cytotoxic activity in cancer cell lines [41]. When applied in vivo against the murine LLC cancer type, FEACYP displayed a capability of inhibiting the tumor growth similar to cisplatin, but with significantly lower side effects. To date, FEACYP is one of only two iron species in the nonendogenous oxidation state + I that have been investigated in vivo, alongside the analogous thiocarbyne complex FETPY (Scheme 1B), which contains a dimethylamino-pyridine ligand. FETPY has demonstrated promising antitumor efficacy with negligible systemic toxicity [42].

The conjugation with bioactive molecules, i.e. structures playing a specific biological role, is a widely investigated and versatile synthetic tool to modify the structure of metallodrugs, since synergy between the bioorganic fragment and the metal center typically results in an enhanced potency [43–47]. Pyridines (i.e., pyridine and substituted pyridines) are found in many natural products and their N-heterocycle skeleton is contained in several FDA-approved pharmaceuticals [48,49]. Moreover, due to their coordination ability, pyridines have been employed as ligands for the design of several anticancer metal complexes [50–53], and may serve as suitable carriers for incorporating organic pharmaceuticals [54,55].

In this work, we report the synthesis, characterization, and investigation of the anticancer potential of novel FEA derivatives, sharing the same N-cyclohexyl aminocarbyne ligand as in FEACYP, and containing a varying pyridine ligand (Scheme 1C).

2. Results and discussion

2.1. Synthesis and characterization of complexes

The μ-aminocarbyne complex $[Fe_2Cp_2(CO)_2(\mu\text{-}CO)\{\mu\text{-}CN(Me)(Cy)\}]CF_3SO_3$, **1**, is readily available from multigram scale synthesis [34]. It can be converted into the mono-acetonitrile adduct **2** using the trimethylamine-N-oxide (TMNO) strategy [56,57]. Complex **2**, which does not require purification for this specific application, undergoes acetonitrile displacement by various pyridines (**py***) in dichloromethane solution (Scheme 2). However, the success of this synthetic procedure is sensitive to the electron-donating capability of the pyridines. Specifically, the reactions with 4-aminopyridine (**ap**) and 4-dimethylaminopyridine (**dmap**) proceeded smoothly at room temperature, while the reactions with pyridine (**py**) and 4-trifluoromethylpyridine (**tfmp**) required reflux conditions for successful completion. The nicotinamide derivative **4** was efficiently obtained avoiding the intermediate formation of **2**, via the one-pot treatment of **1** with **na** in the presence of TMNO. Compounds **3a-c** and **4** were purified using alumina chromatography and were isolated as brown solids in 51–73 % yield. Conversely, **3d** underwent extensive decomposition on alumina, suggesting a relatively weak coordination of **tfmp**. This product was obtained with a low purity in *ca.* 68 % yield, by re-precipitation from the crude reaction mixture.

The FTIR spectra of **3**–**4** (dissolved in CH_2Cl_2) share a characteristic pattern consisting of three bands within the 2300-1500 cm^{-1} range, corresponding to the CO ligands and the carbyne-nitrogen bond (Fig. S1, Table S1). For complex **3a**, these bands are observed at 1982 (terminal

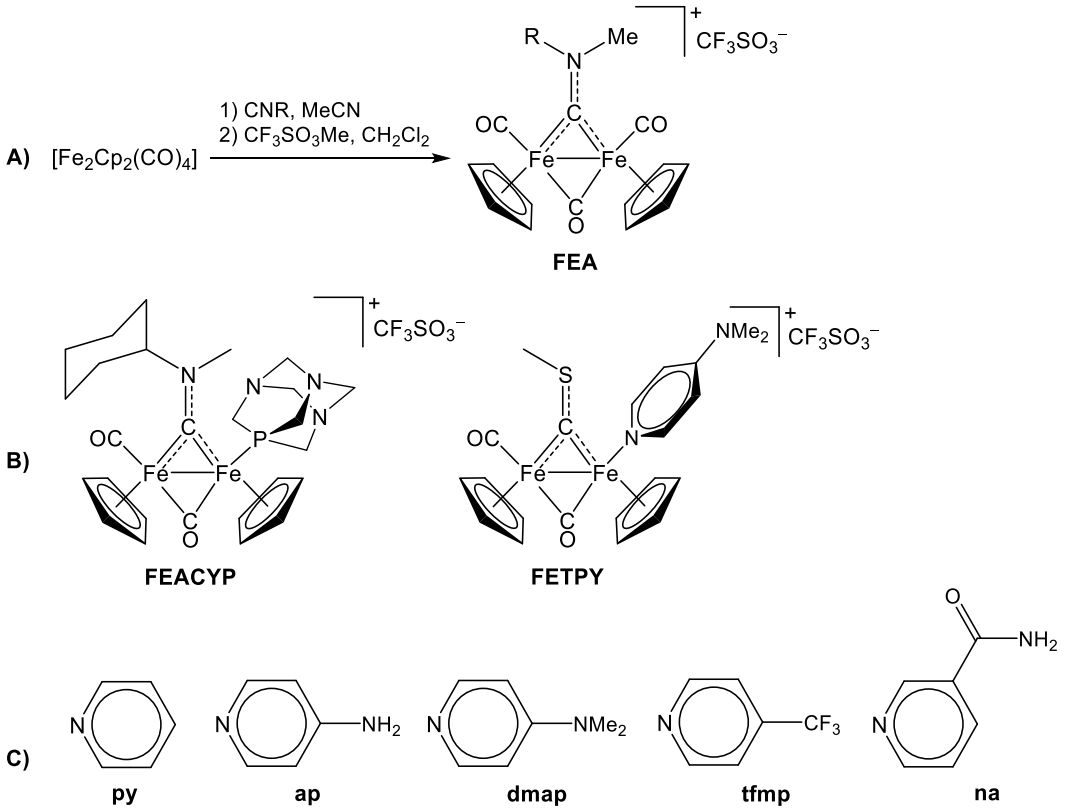

Scheme 1. **A**) Synthesis of diiron (Fe^IFe^I) μ-aminocarbyne complexes (R = aryl or alkyl); **B**) Structures of FEACYP and FETPY**,** showing promising in vivo activity profiles. **C**) Pyridine ligands employed in this work.

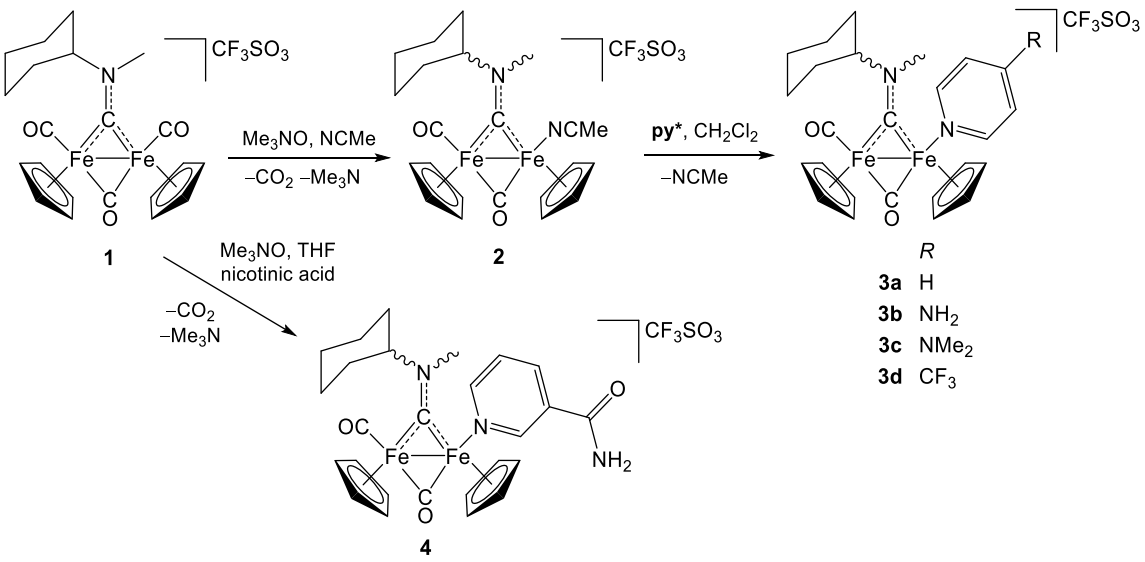

Scheme 2. Synthesis of diiron aminocarbyne complexes with a varying pyridine ligand. Wavy bonds indicate stereoisomerism.

CO), 1798 (bridging CO) and 1525 cm^{-1} (μ-CN). The wavenumber values do not vary appreciably across series **3(a-d)-4**, indicating that the distinct electronic properties of the pyridine ligands do not significantly affect the degree of back-donation from the iron centers to the carbonyl ligands. In contrast, the μ-carbonyl absorptions in the parent complexes occur respectively at 1835 (**1**) [34] and 1818 cm^{-1} (**2**) [56], clearly reflecting the increasing electron-donor nature of the ligands in the series CO < NCMe < pyridine. Increased electron donation to the iron is expected to enhance back-donation to the bridging carbonyl ligand, resulting in a lower wavenumber.

Compounds **3a-d** and **4** were characterized by NMR spectroscopy in $CDCl_3$, acetone-d_6 or CD_3OD solutions (Figs. S2–S23). The ^1H and ^1H 1D-NOESY NMR spectra allowed for a detailed evaluation of the isomers of **3a-c** and **4** in solution. The *cis* arrangement of the Fe_2Cp_2 core is the most favorable for **3**–**4**, although appreciable amounts of *trans* isomers were detected for **3a-c** (*cis/trans* ratio ≈ 3–5). *Cis* and *trans* isomers in diiron aminocarbyne complexes of the formula $[Fe_2Cp_2(CO)(L)(\mu\text{-}CO)\{\mu\text{-}CN(Me)(R)\}]^+$ (L = N-ligand) can be distinguished based on the ^1H NMR chemical shift of the Cp ligands [58,59]. Specifically, the cyclopentadienyl resonances of *trans*-**3a-c** are closer to each other ($\Delta\delta$ = 0–0.070 ppm) and upfield shifted ($\delta \approx$ 4.5–4.7 ppm) with respect to those of the *cis* counterparts ($\Delta\delta$ = 0.12–0.32 ppm, $\delta \approx$ 4.8–5.2 ppm). *E/Z* isomerism relates to the orientations of the aminocarbyne substituents with respect to the N-carbyne bond. This type of isomerism, typically observed in related aminocarbyne complexes, arises from the partial double-bond character of the carbyne-nitrogen bond, which hampers the rotation of the N-substituents around this bond [30,33]. In **3a-c** and **4** (*cis* isomers), the *E* configuration predominates, with *E/Z* molar ratios ranging from 2.4 to 4.0. This feature is associated with steric factors, as the *E* configuration positions the bulky cyclohexyl and pyridyl units further apart from each other. Conversely, the *Z* configuration is prevalent for *trans* isomers.

The ^{13}C NMR spectra of **3**–**4** feature a diagnostic signal for the carbyne carbon, at typically high frequencies. For a detailed comparison, complexes **1**, **2**, **3a** and **3c** (in $CDCl_3$) show this signal at 316.4,[34] 330.5,[56] 332.8 and 333.7 ppm, respectively, reflecting the increasing electron-donor ability in the series CO < NCMe < **py** < **dmap**. This trend is consistent with the observed IR data, that indicate that the Fe → μ-CO back-donation and the Fe → μ-CN back-donation both increase on increasing the electron donation from the variable monodentate ligand (CO, NCMe or pyridine) to the iron. Enhanced back-donation to the μ-CN (Me)(Cy) moiety reinforces its aminocarbyne nature in spite of the iminium character (Fig. 1) [33]. DFT calculations estimate that, in the tris-carbonyl complex **1**, the iminium form (**III**) contributes approximately 50 % to the overall structure [34]. In the ^{13}C NMR spectra of **1**, **2**, **3a** and **3c**, the μ-CO resonance values show a trend similar to that observed for the carbyne (δ/ppm = 255.3,[34] 266.7,[56] 273.4 and 273.4, in the order given).

The molecular structures of **3b** and **3d** were determined through X-ray diffraction analyses (Figs. 2–3, Table 1). Compounds **3b** and **3d** in the solid state retain the *cis*-$[Fe_2Cp_2(\mu\text{-}CO)\{\mu\text{-}CN(Me)(Cy)\}]$ core of **1** and **2** [34,56]. The C(3)–N(1) bond [1.280(9) and 1.278(10) Å for the two independent molecules present within the unit cell of **3b**; 1.302(5) Å for **3d**] shows some π−character in accord to its aminocarbyne/iminium nature, as also found in **1** [1.291(18) Å] [34] and **2** [1.288(7) Å] [56]. The pyridine ligands in **3b** and **3d** are on the same side of the Me-group of μ-CN(Me)(Cy) (*E* isomer), whereas a *Z* configuration was found in the solid state structure of **2** [56]. The bond-lengths in the CO ligands are

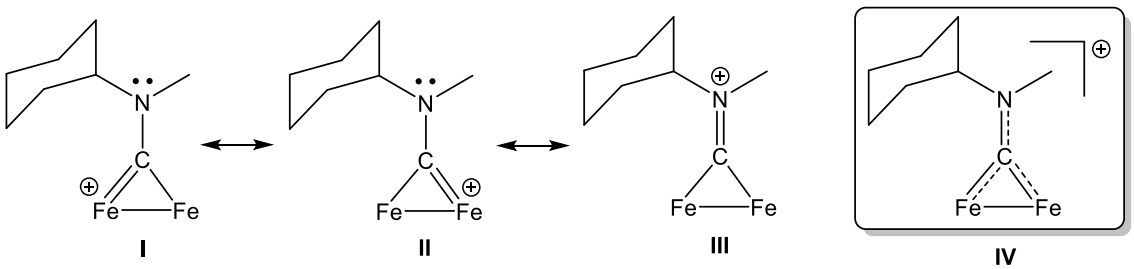

Fig. 1. Resonance forms describing the binding of the bridging {CN(Me)(Cy)} ligand to the $\{Fe_2Cp_2(CO)_3\}$ fragment: **I**, **II**: aminocarbyne forms (back-donation from FeFe); **III**: iminium form. **IV**: comprehensive representation with delocalized positive charge.

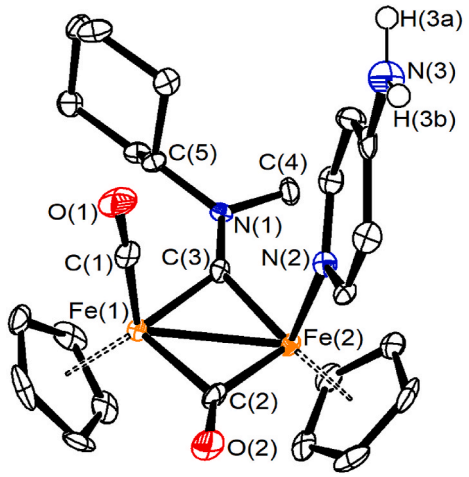

Fig. 2. View of the molecular structure of the cation of **3b**. Displacement ellipsoids are presented at the 50 % probability level. Hydrogen atoms have been excluded for clarity, with the exception of those attached to N(3).

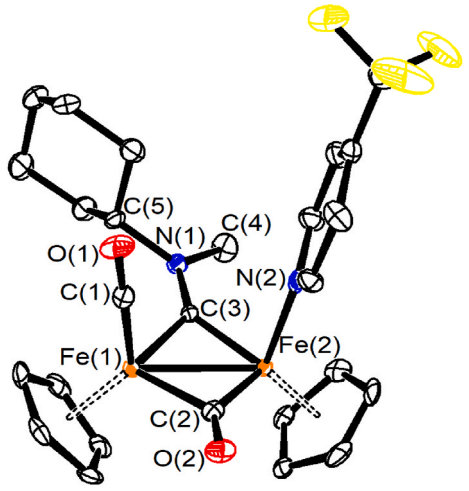

Fig. 3. View of the molecular structure of the cation of **3d**. Displacement ellipsoids are presented at the 50 % probability level. Hydrogen atoms have been excluded for clarity.

considerably longer [1.132(10) to 1.169(4) Å] than in free carbon monoxide [1.128 Å] [60]. In addition, the μ-CO ligand shows a marked asymmetry, as usually found in related diiron complexes displaying different terminal ligands on Fe(1) and Fe(2) [33]. In particular, Fe(1)–C(2) contact [1.976(7) and 1.951(8) Å for **3b**; 1.934(4) Å for **3d**] is considerably longer than Fe(2)–C(2) [1.891(8) and 1.887(8) Å for **3b**; 1.899(4) Å for **3d**], in view of the greater σ-donor character of pyridines compared to CO. This effect is less marked in the case of the bridging aminocarbyne ligand [Fe(1)–C(3) 1.883(8) and 1.885(8) Å for **3b**, 1.875 Å for **3d**; Fe(2)–C(3) 1.857(7) and 1.868(7) Å for **3b**, 1.863(3) Å for **3d**]. A similar trend was observed in the case of **2** [Fe(1)–C(2) 1.969 (6) Å, Fe(2)–C(2) 1.887(6) Å, Fe(1)–C(3)1.884(5) Å, Fe(2)–C(3) 1.961 (5) Å] [56]. For the sake of comparison, the following bonding parameters were found for the symmetrically substituted **1**: Fe(1)–C(2) 1.965 (16) Å, Fe(2)–C(2) 1.924(16) Å, Fe(1)–C(3) 1.873(15) Å, Fe(2)–C(3) 1.881(14) Å [34]. The asymmetry of the μ-CO ligand is less marked in **3d** [{Fe(1)–C(2)} – {Fe(2)–C(2)} 0.044(4) Å] than in **3b** [0.085(8) and 0.064(8) Å] and **2** [0.082(6) Å] [56]. This is likely to be due to the presence of the electron withdrawing CF_3-group in the pyridine ligand of **3d**. Hydrogen bonding is present in the solid-state structure of **3b**, involving the NH_2-group of the cations and the $CF_3SO_3^-$ anions

Table 1
Selected bond lengths (Å) and angles (°) for **3b** and **3d**. *Two independent molecules are present within the unit cell.

		3b*		3d
		Molecule 1	Molecule 2	
Bond lengths (Å)	Fe(1)–Fe(2)	2.5052(15)	2.4888(15)	2.5075(7)
	Fe(1)–C(1)	1.751(8)	1.749(9)	1.765(4)
	Fe(1)–C(2)	1.976(7)	1.951(8)	1.943(4)
	Fe(2)–C(2)	1.891(8)	1.887(8)	1.899(4)
	Fe(1)–C(3)	1.883(8)	1.885(8)	1.875(3)
	Fe(2)–C(3)	1.857(7)	1.868(7)	1.863(3)
	Fe(2)–N(2)	2.024(6)	2.017(6)	2.008(3)
	C(1)–O(1)	1.138(9)	1.132(10)	1.143(4)
	C(2)–O(2)	1.149(9)	1.153(9)	1.169(4)
	C(3)–N(1)	1.280(9)	1.278(10)	1.302(5)
	N(1)–C(4)	1.471(10)	1.477(10)	1.478(5)
	N(1)–C(5)	1.494(9)	1.474(10)	1.495(4)
Bond angles (°)	Fe(1)-C(1)-O(1)	178.0(7)	177.7(8)	178.9(3)
	Fe(1)-C(2)-Fe(2)	80.7(3)	80.8(3)	81.49(14)
	Fe(1)-C(3)-Fe(2)	84.1(3)	83.1(3)	84.26(15)
	Fe(1)-C(3)-N(1)	135.3(6)	134.7(6)	133.8(3)
	Fe(2)-C(3)-N(1)	140.6(6)	142.2(6)	141.9(3)
	C(3)-N(1)-C(4)	122.5(6)	121.8(6)	122.2(3)
	C(3)-N(1)-C(5)	122.2(6)	122.0(7)	121.4(3)
	C(4)-N(1)-C(5)	115.2(6)	116.1(6)	116.3(3)

(Table S2). The structure of **3d** represents the first example of crystallographic characterization of an organoiron-**tfmp** complex [61].

2.2. Solubility and stability in aqueous media, and octanol-water partition coefficients

In preparation for biological studies, the behavior of the pyridine complexes **3**–**4** was evaluated in aqueous solutions using NMR and UV–Vis methods (Table 2). For comparison, the acetonitrile adduct **2** was included in this study. Generally, complexes **3**–**4** exhibit appreciable water solubility (1.1–2.2 mM in D_2O) [62] and a substantial amphiphilic character ($-0.21 < \text{Log } P_{ow} < +0.54$).

The stability of **3**–**4** was assessed under physiological-like conditions using ^{1}H NMR spectroscopy in D_2O and DMEM-d (deuterated cell culture medium) at 37 °C for 72 and 24 h, respectively, with CD_3OD as the co-solvent [63–65]. Overall, complexes **3a-c** demonstrated satisfactory stability in both media, with the dmap derivative **3c** exhibiting the highest stability. Conversely, **3d** and **4** showed greater degradation. In each case, a partial release of the corresponding pyridine ligand was observed (see SI for details). The residual amount of **3a-d** increases with the electron-donating ability of the para-substituent on the pyridyl ring ($CF_3 \ll H < NH_2 < NMe_2$).

Overall, the physicochemical profile of **3a-c** in water resembles that of the tris-carbonyl precursor **1**. Due to the insufficient stability in aqueous media, **3d** was excluded from the biological investigations.

2.3. Biological studies

2.3.1. In vitro cytotoxicity

The *in vitro* cytotoxicity of the diiron complexes **3a-c** and **4** was evaluated against seven human cancer cell lines and the normal MRC-5 cell line to assess selectivity, using the MTT test in the concentration range of 0.1–50 μM. For comparative purposes, the parent diiron complexes **1** and **2** and the anticancer drug cisplatin were also evaluated. The data summarized in Table 3 show that the diiron pyridine complexes act as strong antiproliferative agents, with IC_{50} values generally lower than those of cisplatin. Furthermore, the incorporation of the pyridine moiety provides a beneficial effect compared to complexes with carbon monoxide (**1**) and acetonitrile (**2**). Complex **3c**, which contains 4-dimethylaminopyridine, was the most effective, with an average IC_{50} value of approximately 10 μM against cancer cells, and a selectivity tendency ($IC_{50} \approx 17$ μM in normal MRC-5 cells). Selectivity index (SI)

Table 2
Solubility in D_2O and partition coefficients (Log P_{ow}) of diiron complexes. The residual amount of starting material and released pyridine ligand after 24 h or 72 h at 37 °C in D_2O/CD_3OD or cell culture medium/CD_3OD solution determined by ^1H NMR using Me_2SO_2 as internal standard.

Complex	Solubility/ mol·L^{-1}	Log P_{ow}	D_2O/CD_3OD solutions after 72 h at 37 °C		DMEM-d/CD_3OD solutions after 24 h at 37 °C		water/CD_3OD ratio (v/v)
			Residual amount of complex (%)	Released pyridine ligand	Residual amount of complex (%)	Released pyridine ligand	
1[a]	$6.2\cdot10^{-3}$	−0.46 ± 0.02	75		85		≥14
2	$2.2\cdot10^{-3}$	−0.3 ± 0.1			54 (72 h)		2
3a	$(2.2 \pm 0.1)\cdot10^{-3}$[b]	−0.13 ± 0.03[b]	66	25	72	28	4
3b	$1.4\cdot10^{-3}$	0.15 ± 0.03[b]	68	30	76	28	2
3c	$1.1\cdot10^{-3}$	0.54 ± 0.06	79	20	≈90	7	1.33
3d	N.A.	N.A.	50[c]	30	30[c]	70	2
4	$1.1\cdot10^{-3}$	−0.21 ± 0.02	46	47	≈60	34	3

[a] Data from the literature.[34] Stability tests performed in pure D_2O and in DMEM-d/CD_3OD 14/1 V/V.
[b] Average of two independent experiments.
[c] Average value of ^1H NMR and ^{19}F NMR data (standard deviation ± 2–3 %).

Table 3
IC_{50} values (μM) determined for diiron complexes and cisplatin on human ovarian (A2780 and cisplatin-resistant A2780R), prostate (PC3), lung (A549), breast (MCF-7), bone (HOS) and colorectal (HT-29) cancer cell lines and the normal MRC-5 cell line, after 24 h exposure. The IC_{50} values are given as the mean ± SD. n.d. = not determined. Resistance factor (RF) = IC_{50} (A2780R)/IC_{50} (A2780).

Complex	A2780	A2780R	PC3	A549	MCF-7	HOS	HT-29	MRC-5	RF
1	15.7 ± 3.8	14.5 ± 1.8	n.d.	n.d.	n.d.	n.d.	n.d.	n.d.	0.9
2	17.6 ± 3.3	13.0 ± 1.2	>50	>50	>50	38.0 ± 3.3	>50	37.5 ± 1.0	0.7
3a	5.4 ± 1.5	6.0 ± 1.5	26.8 ± 1.5	13.5 ± 1.8	16.6 ± 3.1	15.7 ± 1.0	30.9 ± 4.0	18.6 ± 2.4	1.1
3b	2.8 ± 0.9	3.9 ± 0.8	18.0 ± 3.1	11.8 ± 2.6	5.9 ± 1.4	16.0 ± 1.8	16.6 ± 1.8	16.2 ± 0.7	1.4
3c	1.4 ± 0.7	1.8 ± 0.4	28.9 ± 3.7	8.1 ± 2.4	5.1 ± 1.3	13.1 ± 1.1	9.7 ± 3.6	16.8 ± 0.6	1.3
4	11.7 ± 1.8	11.6 ± 2.0	32.1 ± 2.6	13.9 ± 1.3	22.8 ± 3.7	17.7 ± 2.1	44.5 ± 3.7	15.7 ± 0.8	1.0
Cisplatin	15.5 ± 0.9	47.1 ± 2.7	>50	>50	33.0 ± 4.1	33.2 ± 4.4	>50	>50	3.0

values, defined as SI = IC_{50} normal cells/IC_{50} cancer cells, were calculated for each complex, specifically comparing MRC-5 healthy cells to the distinct cancer cell lines (see Table S3). Notably, significant SI values those with IC_{50} ratios differing by an order of magnitude, were observed only for MRC-5 cells compared to A2780, A2780R and MCF-7 cancer cells, where **3b** and **3c** showed the highest cytotoxicity. The most relevant SI values are 5.8 (MRC-5/A2780) and 4.2 (MRC-5/A2780R) for **3b**, and 12 (MRC-5/A2780) and 9.3 (MRC-5/A2780R) for **3c**. In the other cases, SI values range between 0.4 and 3, thus indicating insignificant selectivity. Moreover, all tested complexes **1**–**4** showed notable resistance factor (RF) values (Table 3), which ranged from 0.7 to 1.4, considerably better than the value for cisplatin (RF = 3). Overall, complex **4** showed a lower performance compared to **3a-c**, possibly due to its lower lipophilicity (see Table 2). The pyridine molecules **ap**, **dmap** and **na** were inactive in both A2780 and A2780R cell lines up to 50 μM, suggesting that the dissociated ligands do not contribute to the anticancer activity of the diiron complexes **3**–**4**.

To uncover the dynamics of the antiproliferative effect of the diiron complexes in A2780 cells, time-dependent experiments were conducted (Table 4). The data reveal that the cytotoxicity of the nitrile (**2**) and pyridine complexes (**3a-c** and **4**) does not vary significantly over time. Conversely, the cytotoxicity of the parent complex **1** increases dramatically after 24h. The relatively fast cytotoxic activity exerted by **2**–**4** may be attributed to the relatively weak bonding of the nitrogen ligands compared to carbon monoxide, leading to a quicker activation of these complexes. Consistently, our previous findings indicate that CO ligand dissociation from type **1** complexes initiates fragmentation of the diiron complexes, generating reactive species that collectively contribute to the observed antitumor activity [34].

Table 4
IC_{50} values (μM) determined for diiron complexes and cisplatin in A2780 cells after different incubation times.

Complex	24 h	48 h	72 h
1	15.7 ± 3.8	3.7 ± 0.6	2.0 ± 0.1
2	22.9 ± 4.9	19.1 ± 0.7	20.5 ± 1.8
3a	15.0 ± 1.6	14.7 ± 0.7	14.4 ± 1.3
3b	5.0 ± 0.3	3.4 ± 0.3	2.9 ± 0.3
3c	4.7 ± 1.0	3.4 ± 0.4	2.9 ± 0.5
4	19.2 ± 2.0	16.3 ± 0.5	16.2 ± 1.0
Cisplatin	21.4 ± 2.7	11.7 ± 1.2	6.5 ± 0.7

In contrast, time-dependent changes in IC_{50} values for cisplatin show a standard progression, as previously documented [66].

The pyridine complexes **3a-c** and **4** were subjected to targeted experiment to ascertain their mode of action, which will be described below.

2.3.2. Cellular iron uptake

The internalization of iron in A2780 cells was determined using inductively coupled plasma mass spectrometry (ICP-MS) after 2, 6, 12, 24, 48, and 72 h of incubation with the pyridine complexes **3a-c** and **4** at the respective half-maximal inhibitory concentrations (Table 3). The obtained data are visualized in Fig. 4. Complexes **3a** and **4** provided the highest intracellular iron levels in A2780 cells, whereas the more lipophilic complexes **3b** and **3c** resulted in lower iron accumulation with negligible increase over time, although still approximately double compared to the control cells treated with the vehicle alone. Combined, this data suggests that compounds may undergo fragmentation, initiated by nitrogen ligand dissociation, prior to cell internalization; this process could trigger cytotoxic activity, potentially exerted, at least in part, at the membrane level [67,68].

2.3.3. Cellular responses associated with cell death

The cellular effects of complexes **3a-c** and **4** were studied in human

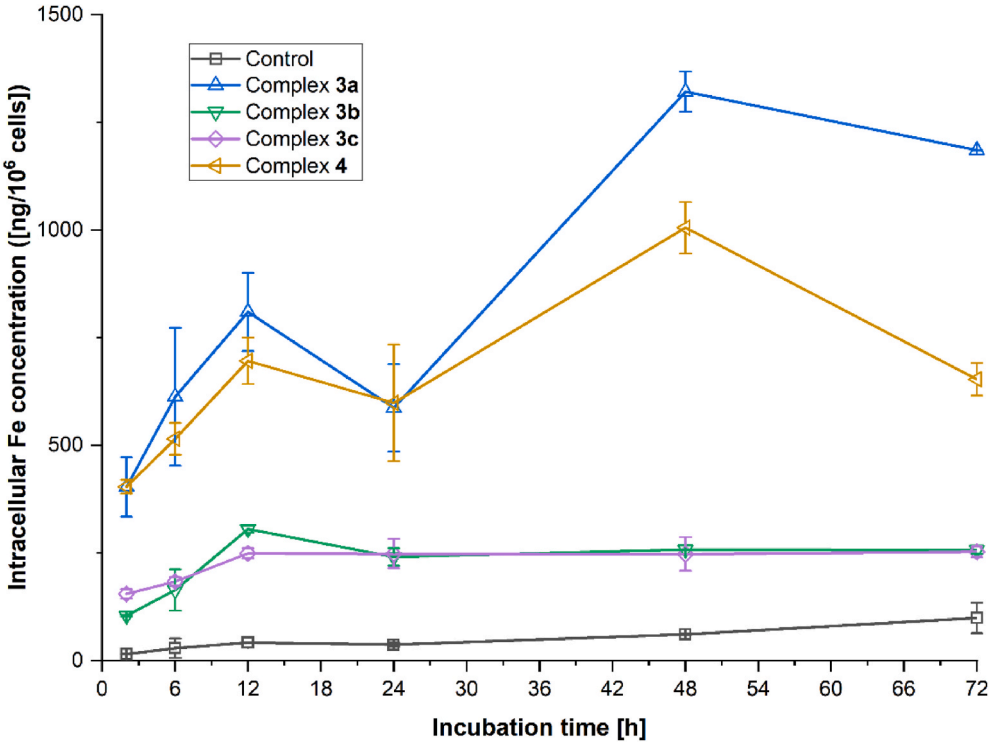

Fig. 4. Iron uptake in A2780 cells after increasing times of incubation with complexes **3a-c** and **4** (ICP-MS).

ovarian cancer cell line A2780 at their half-maximal inhibitory concentrations, as determined by the MTT assay (Table 3), using various flow cytometry methods. The results were compared to those obtained with the therapeutic standard cisplatin.

Initially, the impact of the complexes on the cell cycle was assessed (see Fig. 5A). Unlike cisplatin, a known DNA-binding agent that causes significant cell cycle arrest in the S phase and a marked reduction in the G0/G1 phase population, the iron complexes exhibited a markedly different effect. In fact, they significantly increased the proportion of cells in the G0/G1 phase while reducing the population in the S and G2/M phases, and this phenomenon was particularly evident for **3b** and **4**. Subsequently, apoptosis and/or necrosis in A2780 cells were assessed based on MTT assay data. The Annexin V/PI assay was employed to investigate the cellular effects of the complexes on specific cellular targets, particularly the cellular membrane (which binds Annexin V FITC-conjugated antibodies) and genomic DNA (which interacts with propidium iodide to form a fluorescent product). Among the complexes tested, only **4**, along with the reference drug cisplatin, demonstrated a significant ability to induce both early-stage apoptosis and late-stage apoptosis and/or necrosis in A2780 cells after 24 h of incubation at half-maximal inhibitory concentrations (Fig. 5B). The induction of late-stage apoptosis was further confirmed by the Caspase 3/7 assay, where complex **4** was found to significantly activate Caspase 3/7 after 24 h of incubation (Fig. 5C). In summary, the data from the MTT and flow-cytometry assays suggest that the most active complexes **3a-c** operate through different signaling pathways compared to **4** and cisplatin. The antiproliferative effect of **3a-c** is likely associated with the inhibition of the energetic metabolism of cancer cells.

Then, we moved to evaluate the induction of autophagy. Similar to cisplatin, where autophagy induction is considered a double-edged sword, potentially contributing to both tumor elimination and chemoresistance [69], complexes **3a-c** and **4** induced autophagy in A2780 cells in a modest to moderate degree (Fig. 5D). This suggests that the action of the diiron pyridine complexes on cancer cells is multimodal.

Given that cancer cells are known to undergo unregulated metabolism, leading to intracellular oxidative stress, we caught to analyze the effect of the complexes on oxidative stress induced by the well-known agent pyocyanin [70]. Despite containing redox-active iron centers, the investigated diiron complexes did not contribute to oxidative stress. On the contrary, they alleviated it by 12–23 %, and particularly complex **4** significantly reduced (by 58 %) the levels of reactive oxygen species (ROS) in the cancer cells (see Fig. 6A). In principle, the ancillary ligand nicotinamide (**na**) might contribute to the antioxidant effect of complex **4**, as **na** is known for its antioxidative properties [71]. We hypothesize that the ROS-depleting effect of **4** is likely due to the relatively labile coordination of **na** (Table 2), which facilitates the interaction of the iron centers with potential targets, rather than to the intrinsic biological activity of **na** itself.

Intracellular oxidative stress is often linked to oxidative damage to cellular organelles, such as mitochondria [72,73], leading to disrupted oxidative phosphorylation and intrinsic induction of apoptosis through the sequestration of apoptosome. The effective ROS scavenger **4**, and to a lesser extent complex **3d**, were found to damage the mitochondrial membrane and cause its depolarization (Fig. 6B). This fact suggests that the inhibition of mitochondrial energetic metabolism could be one of the mechanisms through which the investigated diiron complexes induce apoptosis, leading to the death of cancer cells.

3. Conclusions

Diiron bis-cyclopentadienyl complexes with a bridging aminocarbyne ligand are promising anticancer agents, offering several key advantages for drug development, such as straightforward synthesis from cost-effective chemicals, adequate water solubility due to their ionic nature, lipophilicity and biological properties tunable by broad structural variability. In this study, we describe new derivatives obtained by replacing one carbon monoxide ligand with a series of *para*-(**3**) and *meta*-substituted pyridines (**4**). In general, the presence of a donating substituent strengthens the iron binding, resulting in favorable physicochemical properties in aqueous media and enhanced anticancer activity compared to the pyridine-lacking precursor (**1**). The incorporation of the pyridine moiety introduces a distinct mode of action: while

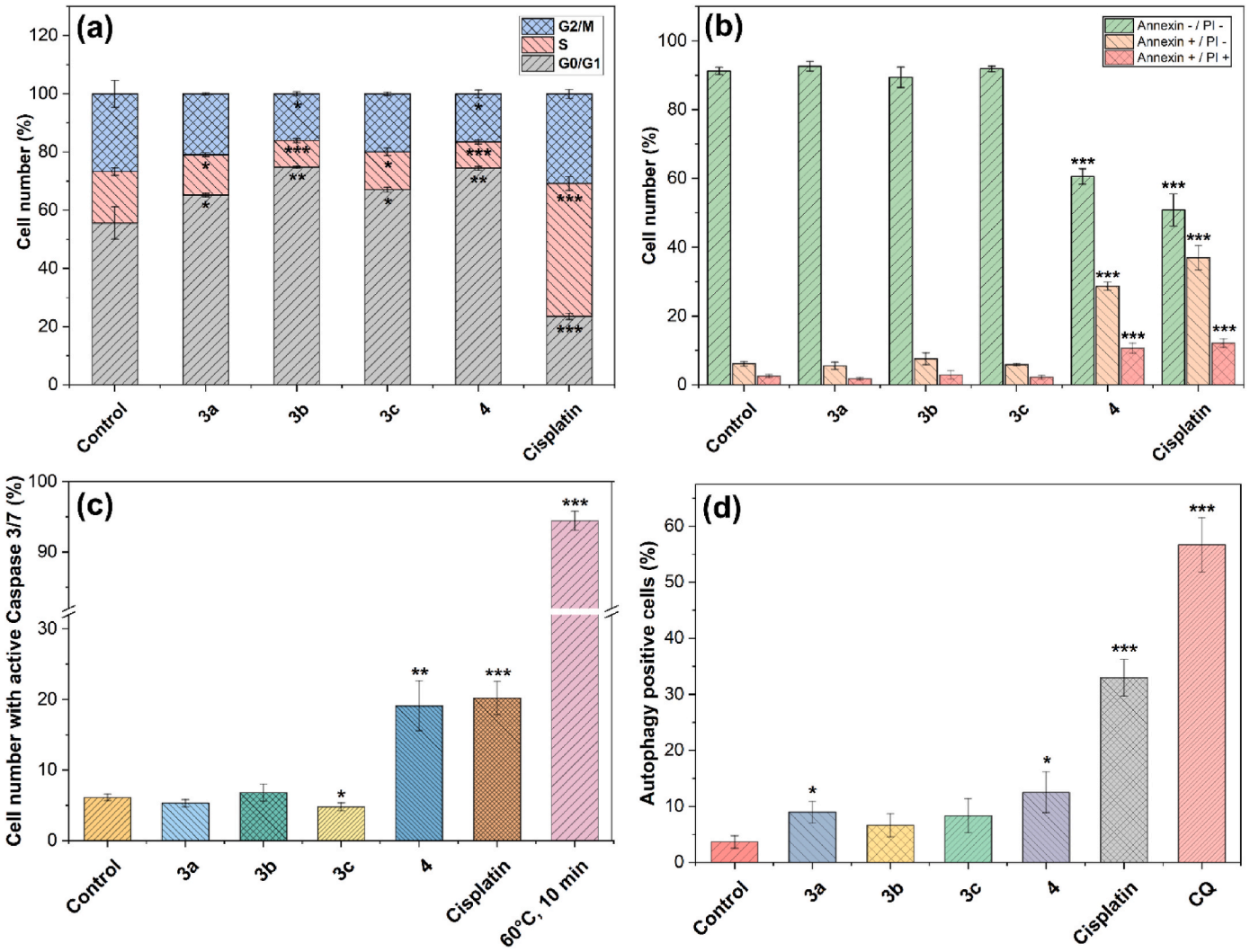

Fig. 5. Cellular effects of **3a-c** and **4** and cisplatin on A2780 cells incubated with half-maximal inhibitory concentrations of the complexes for 24 h. In all cases, control cells were treated with the vehicle alone. (**a**) Flow-cytometric analysis of the cell cycle in A2780 cells; (**b**) Annexin V/PI assay; (**c**) induction of executioner caspases 3/7; (**d**) induction of autophagy. The abbreviation CQ refers to the positive control, where cells were treated with a mixture of chloroquine (10 μM) and rapamycin (0.5 μM).

1 and its analogues were previously found to disrupt cell redox homeostasis by increasing intracellular ROS levels, **3**–**4** may inhibit cancer cell metabolic processes through moderate to strong ROS depletion, leading to G0/G1 cell cycle arrest. Notably, the nature of the pyridine ligand, presumably associated with its dissociation rate, influences the cellular effects of the diiron complex, indicating the potential for further development of this class of compounds to target specific biological features. Current studies highlight that incorporating 4-dimethylaminopyridine as a ligand in diiron hetero-carbyne complexes (see also FETPY structure in Scheme 1B) could be a promising strategy for designing effective anticancer agents.

CRediT authorship contribution statement

Annachiara Rossi: Investigation. **Lorenzo Biancalana:** Data curation. **Ján Vančo:** Investigation. **Tomáš Malina:** Investigation. **Stefano Zacchini:** Investigation, Data curation. **Zdeněk Dvořák:** Investigation. **Zdeněk Trávníček:** Writing – review & editing, Writing – original draft, Supervision, Funding acquisition. **Fabio Marchetti:** Writing – review & editing, Writing – original draft, Supervision, Funding acquisition.

4. Experimental

4.1. General details

Organic reagents were purchased from Merck or TCI Europe, and were of the utmost available purity. Solvents were obtained from Merck (petroleum ether with a boiling point range of 40–60 °C) and underwent drying using the solvent purification system mBraun MB SPS5. Complexes **1** [34] and **2** [56] were prepared according to the literature. Reactions and chromatographic purifications were carried out in air using standard Schlenk techniques and solvents were used from the bottle. Once isolated, products were stored in air. Separations were carried out on columns of deactivated alumina (Merck, 4 % *w/w* water). Infrared spectra of solutions were recorded on a PerkinElmer Spectrum 100 FTIR spectrometer with a CaF_2 liquid transmission cell (2300-1500 cm^{-1} range). UV–Vis spectra were recorded on an Ultraspec 2100 Pro spectrophotometer. FTIR and UV–Vis spectra were processed with Spectragryph software [74]. NMR spectra were recorded at 298 K on a Jeol YH400 MHz instrument equipped with a Royal HFX Broadband probe. Chemical shifts (expressed in parts per million) are referenced to the residual solvent peaks (^1H, ^{13}C) [75]. ^1H and ^{13}C spectra were assigned with the support of ^1H NOESY (mix time 750 ms, relaxation

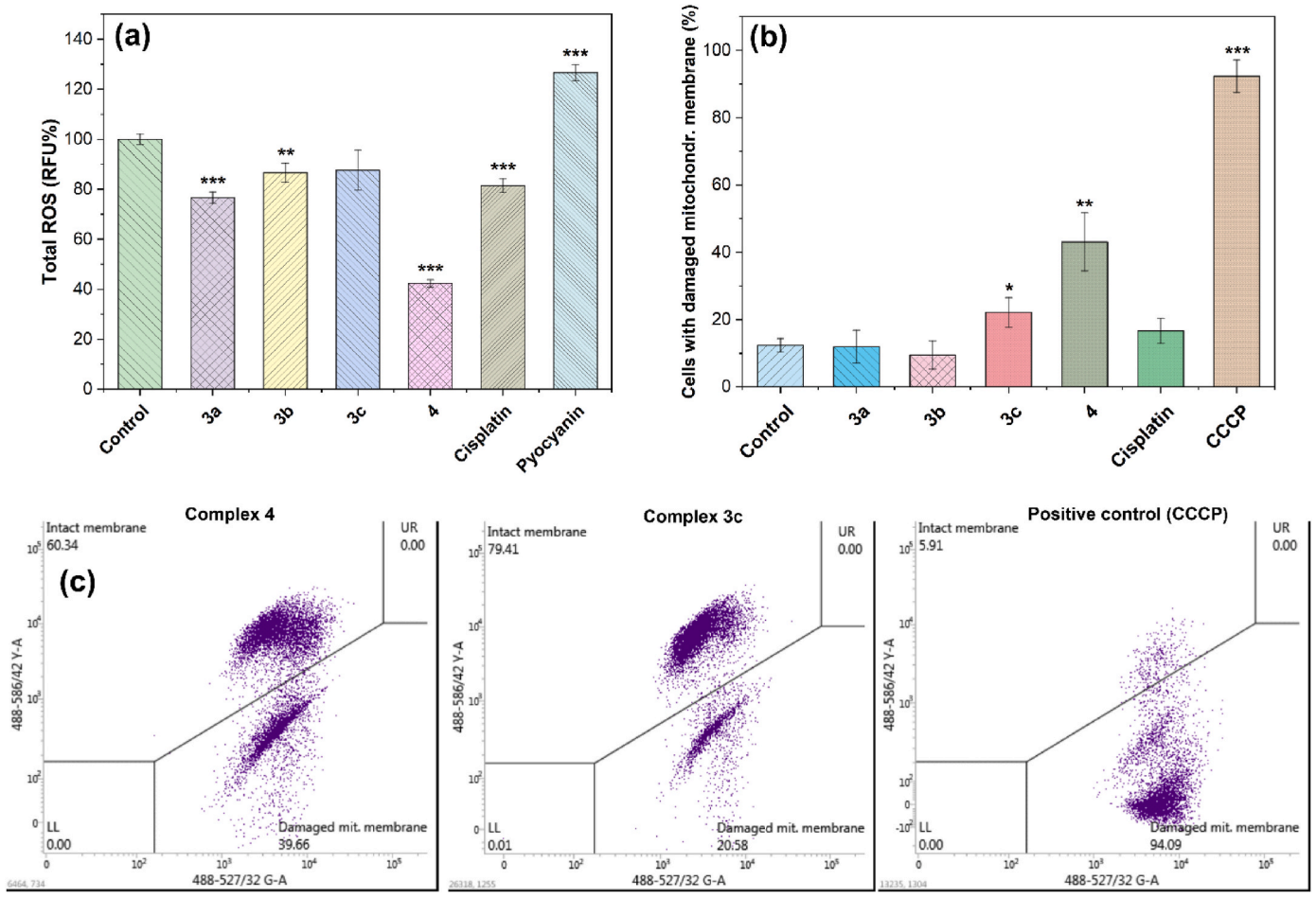

Fig. 6. (**a**) Effect of complexes **3a-c** and **4** and cisplatin on the intracellular levels of reactive oxygen species (ROS) in A2780 cells after the induction of oxidative stress by pyocyanin; (**b**) effect of the tested complexes on the depletion of mitochondrial membrane potential ($\Delta\Psi_m$). The controls refer to the results obtained for vehicle-treated cells, with carbonyl cyanide *m*-chlorophenyl hydrazone (CCCP) serving as the positive control for $\Delta\Psi_m$. (**c**) Dot-plot diagrams from one of the three parallel determinations of $\Delta\Psi_m$, showing the effects of co-incubating A2780 cells with complexes **3c** and **4** and the positive control (CCCP).

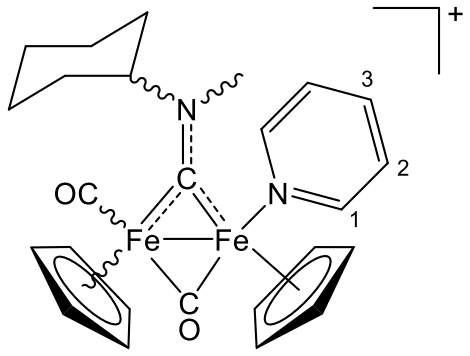

Chart 1. Structure of the cation of **3a** (*cis-trans* and *E-Z* isomers).

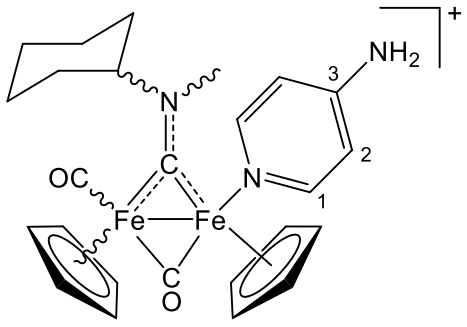

Chart 2. Structure of the cation of **3b** (*cis-trans* and *E-Z* isomers).

time 1 s, linewidth 25 Hz) and $^{1}H–^{13}C$ *gs*-HSQC experiments. The cyclopentadienyl ligand bonded to the same iron as the *N*-donor ligand is labeled as Cp^{N}. NMR signals due to minor isomeric forms are italicized. Elemental analyses were performed on a Vario MICRO cube instrument (Elementar).

4.2. Synthesis and characterization of diiron complexes [$Fe_2Cp_2(CO)(py^*)(\mu\text{-}CO)\{\mu\text{-}CN(Me)(Cy)\}]CF_3SO_3$, 3a-d

General procedure. A dichloromethane solution (ca. 15 mL) of complex **2**, freshly prepared from **1** and Me_3NO in acetonitrile [56], was treated with the appropriate py* reagent (1.3–2.0 equivalents). The resultant mixture obtained was stirred at reflux for 3 h (**3a**, **3d**) or at room temperature for 18 h (**3b**, **3c**). Subsequently, the mixture underwent a purification procedure. For samples **3a-c**, the crude reaction mixture was transferred onto an alumina column. Elution with CH_2Cl_2 and a CH_2Cl_2/THF mixture (3:2 v/v) allowed the separation of impurities. A band, corresponding to the product, was then eluted using a THF/MeOH mixture (6:1 v/v; **3a**) or a CH_3CN/MeOH mixture (9:1 v/v; **3b,c**). The eluate was dried under vacuum. For **3d**, the crude reaction mixture was filtered through a Celite pad. The filtrate solution was

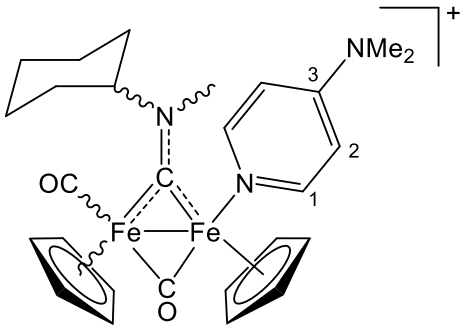

Chart 3. Structure of the cation of **3c** (*cis-trans* and *E-Z* isomers).

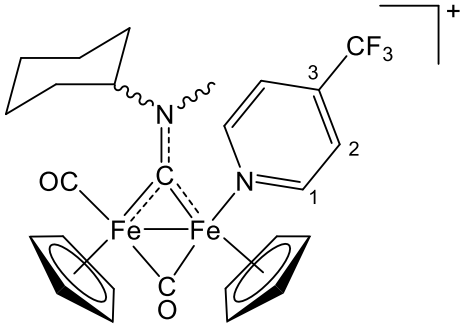

Chart 4. Structure of the cation of **3d** (*E* and *Z* isomers).

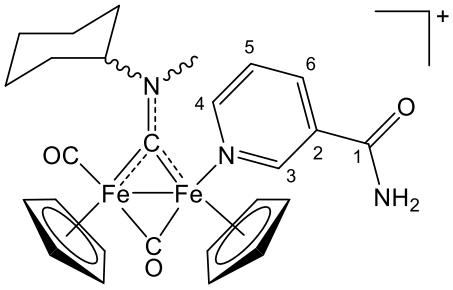

Chart 5. Structure of the cation of **4** (*E* and *Z* isomers).

evaporated under reduced pressure. The resulting solid residue was sequentially suspended in the following solvents and filtered: Et_2O (15 mL) for 1–12 h, toluene (15 mL) for 10–30 min and pentane (15 mL) for 30 min. Volatile components were evaporated under reduced pressure, and the residue was reprecipitated using a CH_2Cl_2/petroleum ether mixture (ca. 1:15 v/v). Finally, the residue was dried under vacuum.

4.2.1. *[Fe_2Cp_2(CO)(py)(μ-CO){μ-CN(Me)(Cy)}]CF_3SO_3, 3a (Chart 1)*

From **1** (97 mg, 0.162 mmol) and pyridine (30 μL, 0.22 mmol). Following alumina chromatography, the brown residue was washed and then triturated with Et_2O/hexane 1:1 v/v to a powder. The suspension was filtered and the solid was dried under vacuum. Dark brown solid, yield 74 mg (70 %). Soluble in CH_3CN, CH_2Cl_2, chloroform, acetone and slightly soluble in Et_2O and toluene, insoluble in hexane. Anal. calcd. for $C_{26}H_{29}F_3Fe_2N_2O_5S$: C, 48.02; H, 4.50; N, 4.31; S, 4.93. Found: C, 47.73; H, 4.68; N, 4.12; S, 5.10. FTIR (CH_2Cl_2): ũ/cm^{-1} = 1982vs (CO), 1799s (μ-CO), 1526w (μ-CN). ^{1}H NMR ($CDCl_3$): *δ*/ppm for *cis* isomers = 8.19, *8.14* (d, $^3J_{HH}$ = 5.4 Hz, 2H, H^1); *7.49,* 7.44 (t, $^3J_{HH}$ = 7.6 Hz, 1H, H^3); 6.98, *6.95* (m, 2H, H^2); *5.98*, 4.99* (m, 1H, CH^{Cy}); *5.06*, 4.96 (s, 5H, Cp); 4.90, *4.28* (s, 3H, NMe); 4.84, *4.76* (s, 5H, Cp^N); *δ*/ppm for *trans* isomers = 8.55, *8.34* (d, $^3J_{HH}$ = 4.4 Hz, 2H, H^1); 7.22 (m, 2H, H^2); 4.67, *4.29* (s, 3H, NMe); *4.67***, 4.57 (s, 5H, Cp); *4.61*, 4.50 (s, 5H, Cp^N); *δ*/ppm for all isomers = 2.67 (d, *J* = 12 Hz), 2.39–1.96, 1.55–1.29 (m) (10H, CH_2^{Cy}); *cis-E/cis-Z/trans-Z/cis-E* ratio = 73:18:8:3, *cis-E/cis-Z* ratio = 4.0; *cis/trans* ratio = 4.8. *Hidden by Cp resonances. **Hidden by NCH_3 resonance. $^{13}C\{^1H\}$ NMR ($CDCl_3$): *δ*/ppm for *cis* isomers = 332.9 (μ-CN); 273.5 (μ-CO); 211.4 (CO); *155.4*, 155.2 (C^1); 137.6, *137.2* (C^3); 125.0, *124.9* (C^2); *89.7*, 89.2 (Cp); 87.3, *86.91* (Cp^N); 79.3, *77.4* (CH^{Cy}); *47.3****, 45.6*** (NMe); *32.8*, 31.2, 26.24, 26.15, 26.0 (CH_2^{Cy}); *δ*/ppm for *trans* isomers = 89.8, *88.8*, 86.95 (Cp + Cp^N). ***Identified via ^1H–^{13}C HSQC. ^{19}F NMR ($CDCl_3$): *δ*/ppm = −78.1.

4.2.2. *[Fe_2Cp_2(CO)(ap)(μ-CO){μ-CN(Me)(Cy)}]CF_3SO_3, 3b (Chart 2)*

From **1** (120 mg, 0.200 mmol) and **ap** (28 mg, 0.30 mmol). Brown solid, yield 97 mg (73 %). Soluble in MeOH, CH_3CN, CH_2Cl_2 and acetone. Anal. calcd. for $C_{26}H_{30}F_3Fe_2N_3O_5S$: C, 46.94; H, 4.55; N, 6.32; S, 4.82. Found: C, 47.21; H, 4.43; N, 6.15; S, 4.85. *FTIR* (CH_2Cl_2): ũ/cm^{-1} = 1982vs (CO), 1798s (μ-CO), 1639s (NH_2), 1620m-sh (NH_2), 1524m-sh (μ-CN), 1518s. ^{1}H NMR (acetone-d_6): *δ*/ppm for *cis* isomers = 7.56–7.46 (m, 2H, H^1); 6.34–6.29 (m, 2H, H^2); 6.08 (s-br, 2H, NH_2); *6.20**, 5.20* (m, 1H, CH^{Cy}); *5.16*, 5.13 (s, 5H, Cp); 4.93, *4.89* (s, 5H, Cp^N); 4.91, *4.34* (s, 3H, NMe); *δ*/ppm for *trans* isomers = 7.80, *7.72* (d, $^3J_{HH}$ = 6.0–6.5 Hz, 2H, H^1); 6.39 (m, 2H, H^2); 6.18 (s-br, 2H, NH_2); 5.34 (m, 1H, CH^{Cy}); 4.99, *4.36* (s, 3H, NMe); 4.743, *4.736* (s, 5H, Cp); *4.72*, 4.69 (s, 5H, Cp^N); *δ*/ppm all isomers = 2.73–2.10 (m, 4H), 2.01–1.34 (m, 6H) (CH_2^{Cy}); *cis-E/cis-Z/trans-Z/cis-E* ratio = 58:19:16:7; *cis-E/cis-Z* ratio = 3.0, *cis/trans* ratio = 3.3. *Partially overlapped with an adjacent resonance. $^{13}C\{^1H\}$ NMR (acetone-d_6): *δ*/ppm for *cis* isomers = 335.4 (μ-CN); 272.3 (μ-CO); 213.3, *212.2* (CO); 156.3, *155.7* (C^3); *155.0*, 154.7 (C^1); *111.5*, 111.2 (C^2); *90.1*, 89.8 (Cp); 87.7, *87.5* (Cp^N); 79.0, *76.5* (CH^{Cy}); *47.6,* 45.7 (NMe); *33.4*, *32.8*, 31.8, 31.4, *26.43*, 26.40, 26.3, *26.2*, *26.1*, 25.9 (CH_2^{Cy}); *δ*/ppm for *trans* isomers = 111.1 (C^2); *156.3*, 156.07 (C^1); *90.7*, 90.4, 89.7, *89.1* (Cp + Cp^N); 78.6 (CH^{Cy}); *47.3,* 45.4 (NMe); *33.3*, *32.3*, 32.2, 31.6, 26.5 (CH_2^{Cy}). ^{19}F NMR ($CDCl_3$): *δ*/ppm = −78.1. Crystals of **3b** suitable for X-ray analysis were obtained from the slow diffusion of a layer of diethyl ether into an acetone-d_6 solution, at −30 °C.

4.2.3. *[Fe_2Cp_2(CO)(dmap)(μ-CO){μ-CN(Me)(Cy)}]CF_3SO_3, 3c (Chart 3)*

From **1** (120 mg, 0.200 mmol) and **dmap** (32 mg, 0.26 mmol). Dark brown solid, yield 92 mg (66 %). Soluble in CH_3CN, CH_2Cl_2, chloroform, THF, slightly soluble in toluene and insoluble in Et_2O. Anal. calcd. for $C_{28}H_{34}F_3Fe_2N_3O_5S$: C, 48.50; H, 4.94; N, 6.06; S, 4.62. Found: C, 48.31; H, 5.04; N, 5.84; S, 4.55. FTIR (CH_2Cl_2): ũ/cm^{-1} = 1979vs (CO), 1797s (μ-CO), 1626s, 1602m-sh, 1536s, 1525 m (μ-CN). ^{1}H NMR ($CDCl_3$): *δ*/ppm for *cis* isomers = 7.47, *7.43* (d, $^3J_{HH}$ = 7.3 Hz, 2H, H^1); 6.12, *6.08* (d, $^3J_{HH}$ = 7.3 Hz, 2H, H^2); *5.98* (ddt, *J* = 11.7, 7.8, 3.8), 4.99* (m) (1H, CH^{Cy}); *4.98*, 4.90 (s, 5H, Cp); 4.84, *4.25* (s, 3H, NMe); 4.74, *4.66* (s, 5H, Cp^N); *2.88*, 2.86 (s, 6H, NMe_2); *δ*/ppm for *trans* isomers = 7.77 (br.), *7.61* (d, $^3J_{HH}$ = 6.6 Hz) (2H, H^1); 6.38, *6.28* (d, $^3J_{HH}$ = 6.8–7.1 Hz) (2H, H^2); *6.17**, 5.13 (m, 1H, CH^{Cy}); *4.59*, 4.52, *4.51* (s, 10H, Cp + Cp^N); 4.91, *4.26* (s, 3H, NMe); *2.92*, 2.90 (s, 6H, NMe_2); *δ*/ppm for all isomers = 2.67–2.56, 2.32–1.69, 1.56–1.27 (m, 10H, CH_2^{Cy}); *cis-E/cis-Z/trans-Z/cis-E* ratio = 67:16:13:4, *cis-E/cis-Z* ratio = 4.0; *cis/trans* ratio = 4.9. *Partially hidden by adjacent resonance. $^{13}C\{^1H\}$ NMR ($CDCl_3$): *δ*/ppm for *cis* isomers = 333.7, *333.3* (μ-CN); 273.4, *272.0* (μ-CO); 211.6, *211.2* (CO); *154.0*, 153.9 (C^3); *153.3*, 153.1 (C^1); 108.2, *108.0* (C^2); *89.3*, 88.8 (Cp); 87.0, *86.5* (Cp^N); 78.9, *76,3* (CH^{Cy}); *47.4,* 45.5 (NMe); *39.13*, 39.08 (NMe_2); *32.9*, *32.6*, 31.3, 31.1, *26.3*, 26.23, 26.16, *26.09*, *25.4*, 25.26 (CH_2^{Cy}); *δ*/ppm for *trans* isomers = 332.6 (μ-CN); 270.5 (μ-CO); 211.8 (CO); 154.1 (C^3); 154.6 (C^1); 109.0, *108.9* (C^2); *90.0*, 89.6, 88.6, *87.9* (Cp + Cp^N); 78.5 (CH^{Cy}); *47.0*, 45.3 (NMe); 39.2 (NMe_2); 31.8, 30.9, 30.4, 26.0, 25.31 (CH_2^{Cy}); *δ*/ppm = 121.1 (d, $^1J_{CF}$ = 321 Hz, CF_3SO_3). ^{19}F NMR ($CDCl_3$): *δ*/ppm = −78.0.

4.2.4. *[Fe_2Cp_2(CO)(tfmp)(μ-CO){μ-CN(Me)(Cy)}]CF_3SO_3, 3d (Chart 4)*

From **1** (150 mg, 0.250 mmol) and **tfmp** (58 μL, 0.50 mmol). Brown solid, yield 120 mg (67 %). Soluble in MeOH, CH_3CN, CH_2Cl_2,

chloroform, THF, slightly soluble in toluene and Et_2O. FTIR (CH_2Cl_2): ũ/cm^{-1} = 1983vs (CO), 1802s (μ-CO), 1540w, 1528w (μ-CN). ^{1}H NMR (CD_3OD): *δ*/ppm = *8.82*, 8.48 (d, $^3J_{HH}$ = 4.6–5.2 Hz, 2H, H^1); 7.73, 7.39 (d, $^3J_{HH}$ = 4.7–5.3 Hz, 2H, H^2); *6.06* (m, 1H, CH^{Cy}); *5.13*, 5.11 (s, 5H, Cp); 4.93 (s, 5H, Cp^N); 4.84, *4.30* (s, 3H, NCH_3); *cis-E/cis-Z* ratio = 12. ^{19}F NMR (CD_3OD): *δ*/ppm = − *66.79*, −66.84 (Py-CF_3); - 80.0 (CF_3SO_3). Crystals of **3d** suitable for X-ray analysis were obtained from the slow diffusion of a layer of diethyl ether into a CH_2Cl_2 solution stored at −30 °C.

4.3. Synthesis and characterization of [Fe_2Cp_2(CO)(na)(μ-CO){μ-CN(Me)(Cy)}]CF_3SO_3, 4 (Chart 5)

A solution of **1** (95 mg, 0.16 mmol) in tetrahydrofuran (20 mL) was treated with nicotinamide (**na**; 29 mg, 0.24 mmol), followed by the addition of $Me_3NO{\cdot}2H_2O$ (35 mg, 0.32 mmol). The mixture was allowed to stir at room temperature for 18h, during which the generated gas was allowed to escape. Hence, the volatile components were evaporated under reduced pressure. The resulting residue was dissolved in the minimum volume of dichloroethane, and this solution was loaded onto an alumina column. Elution with a CH_2Cl_2/THF mixture (3:2 v/v) enabled the separation of impurities. A dark green band, corresponding to the desired product, was eluted using a MeCN/MeOH mixture (9:1 v/v). Volatiles were evaporated under reduced pressure and the product was reprecipitated using a CH_2Cl_2/petroleum ether (ca. 1:15 v/v) mixture. The obtained solid was dried under vacuum. Dark green solid, yield 57 mg (51 %). Soluble in MeOH, CH_3CN, CH_2Cl_2 and acetone. Anal. calcd. for $C_{27}H_{30}F_3Fe_2N_3O_6S$: C, 46.78; H, 4.36; N, 6.06; S, 4.63. Found: C, 46.56; H, 4.49; N, 6.18; S, 4.52. FTIR (CH_2Cl_2): ũ/cm^{-1} = 1985vs (CO), 1800s (μ-CO), 1688s (C^1O), 1614w (NH_2), 1525w (μ-CN). ^{1}H NMR (acetone-d_6): *δ*/ppm = 8.86 (m, $^3J_{HH}$ = 8.6 Hz, 1H, H^4); 8.41, *8.38* (s, 1H, H^3); 8.10, *8.08* (m, 1H, H^6); 7.65 (br, 1H, NH_2); 7.29 (m, 1H, H^5); 6.98 (br, 1H, NH_2); *6.22*, 5.21* (m, 1H, CH^{Cy}); *5.24*, 5.21 (s, 5H, Cp); 5.06, *5.02* (s, 5H, Cp^N); 4.98, *4.41* (s, 3H, NMe); 2.65 (d), 2.35–2.13, 2.00–1.25 (m, 10H, CH_2^{Cy}); *cis-E/cis-Z* ratio = 2.4. *Hidden by Cp resonances. $^{13}C\{^1H\}$ NMR (acetone-d_6): *δ*/ppm = 334.1 (μ-CN); 272.4 (μ-CO); 212.8 (CO); *165.3*, 165.1 (C^1); *158.8*, 158.7 (C^4); *156.3*, 156.1 (C^3); *136.6*, 136.5 (C^6); 131.1 (C^2); 125.0, *124.9* (C^5); *90.6*, 90.2 (Cp); 88.1, *87.8* (Cp^N); 79.5, *76.9* (CH^{Cy}); *48.1*, 46.1 (NMe); *33.7*, *35.2*, 31.8, 31.6, *26.5*, 26.43, *26.39*, 26.3, *26.1*, 25.9 (CH_2^{Cy}). ^{19}F NMR ($CDCl_3$): *δ*/ppm = −78.7.

4.4. X-ray crystallography

Crystal data and collection details for **3b**·0.5CH_3COCH_3 and **3d**·0.5CH_2Cl_2 are reported in Table 5. Data were recorded on a Bruker APEX II diffractometer equipped with a PHOTON2 detector using Mo–Kα radiation. The structures were solved by direct methods and refined by full-matrix least-squares based on all data using F^2 [76]. Hydrogen atoms were fixed at calculated positions and refined using a riding model.

Table 5
Crystal data and measurement details for **3b**·0.5CH_3COCH_3 and **3d**·0.5CH_2Cl_2.

	3b·0.5CH_3COCH_3	3d·0.5CH_2Cl_2
Formula	$C_{27.5}H_{33}F_3Fe_2N_3O_{5.5}S$	$C_{27.5}H_{29}ClF_6Fe_2N_2O_5S$
FW	694.33	760.74
T, K	100(2)	100(2)
λ, Å	0.71073	0.71073
Crystal system	Triclinic	Monoclinic
Space group	$P\bar{1}$	*C2/c*
a, Å	13.9183(13)	28.7223(17)
b, Å	14.3038(14)	11.5014(7)
c, Å	17.1557(17)	20.9907(11)
α,°	80.230(4)	90
β,°	77.396(4)	121.282(2)
γ,°	63.073(3)	90
Cell Volume, Å^3	2961.9(5)	5926.1(6)
Z	4	8
D_c, g•cm^{-3}	1.557	1.705
μ, mm^{-1}	1.113	1.220
F(000)	1432	3096
Crystal size, mm	0.16 × 0.14 × 0.10	0.19 × 0.18 × 0.13
θ limits,°	1.602–25.049	1.659–25.995
Reflections collected	32362	37417
Independent reflections	10092 [R_{int} = 0.0751]	5800 [R_{int} = 0.0472]
Data/restraints/parameters	10092/60/761	5800/72/413
Goodness on fit on F^2[a]	1.189	1.119
R_1 ($I > 2\sigma(I)$)[b]	0.0824	0.0533
wR_2 (all data)[c]	0.1882	0.1055
Largest diff. peak and hole, e Å^{-3}	1.031/−0.722	0.923/−0.586

[a] Goodness on fit on $F^2 = [\Sigma w(F_O^2 - F_C^2)^2/(N_{ref} - N_{param})]^{1/2}$, where $w = 1/[\sigma^2(F_O^2) + (aP)^2 + bP]$, where $P = (F_O^2 + 2F_C^2)/3$; N_{ref} = number of reflections used in the refinement; N_{param} = number of refined parameters.
[b] $R_1 = \Sigma||F_O| - |F_C||/\Sigma|F_O|$.
[c] $wR_2 = [\Sigma w(F_O^2 - F_C^2)^2/\Sigma w(F_O^2)^2]^{1/2}$, where $w = 1/[\sigma^2(F_O^2) + (aP)^2 + bP]$, where $P = (F_O^2 + 2F_C^2)/3$.

4.5. Behavior in aqueous media

4.5.1. Solubility in water (D_2O)

The selected compound was suspended in a D_2O solution (0.70 mL) containing dimethyl sulfone (Me_2SO_2; 4.04·10^{-3} M) and stirred at room temperature (22 ± 2 °C) for 3 h. The saturated solution was filtered over Celite and analyzed by ^{1}H NMR (delay time = 10 s; number of scans = 20). The concentration (=solubility) was calculated by the relative integral with respect to Me_2SO_2 as the internal standard [*δ*/ppm = 3.14 (s, 6H)] (Table 2). NMR data are reported in the Supporting Information.

4.5.2. Octanol/water partition coefficient (Log P_{ow})

Partition coefficients (P_{ow}), defined as $P_{ow} = c_{org}/c_{aq}$, where c_{org} and c_{aq} are the molar concentrations of the selected compound in the n-octanol and aqueous phase, respectively, were determined by the shake-flask method and UV–Vis measurements, according to a previously described procedure [77,78]. All operations were carried out at room temperature (22 ± 2 °C). The stock solutions of **3a-c** were prepared in water-saturated octanol, and the stock solution of **4** in octanol-saturated water. The wavelength corresponding to a well-defined maximum of shoulder absorption of each compound (305–400 nm range) was used for UV–Vis quantitation. The procedure was repeated three times for each sample (from the same stock solution); results are given as mean ± standard deviation (Table 2).

4.5.3. Stability in CD_3OD/D_2O mixture

The selected compound (*ca.* 5 mg) was dissolved in CD_3OD then diluted with a D_2O solution containing 4.04 x 10^{-3} M dimethylsulfone (Me_2SO_2) as internal standard up to 0.70–0.80 mL total volume. The resulting solution (D_2O/CD_3OD volume ratios: 4 for **3a**, 3 for **4**, 2 for **3b, d**, 1.33 for **3c**; $c^0_{Fe2} \approx$ 1 x 10^{-2} mol/L) was filtered over Celite, then transferred into an NMR tube and the ^{1}H NMR spectrum was recorded. The mixture was maintained at 37 °C for 72 h. After filtration over Celite, the solution was re-analyzed by ^{1}H NMR. The residual amount of starting material in the final solution and the amount of pyridine ligand released, with respect to the initial spectrum, were calculated by the relative integral with Me_2SO_2 as the internal standard (Table 2). NMR spectra were recorded using the following settings: number of scans = 20; relaxation delay = 4 s. NMR data are reported in the Supporting Information.

4.5.4. Stability in CD_3OD/DMEM mixture

Deuterated cell culture medium (DMEM-d) was prepared by dissolving powdered DMEM cell culture medium (1000 mg/L glucose and L-glutamine, without sodium bicarbonate and phenol red; D2902 - Sigma Aldrich) in D_2O (10 mg/mL, according to the manufacturer's instructions). The solution was treated with Me_2SO_2 (*ca.* 6·10^{-3} M),

NaH_2PO_4 and Na_2HPO_4 (25 mM total phosphate, pD = 7.4 [79]), then stored under N_2. Solutions of Fe compounds in a DMEM-d/CD_3OD mixture were prepared, treated and analyzed as described above. Data is reported in Table 2 and Supporting Information.

4.6. Biological studies

4.6.1. Antiproliferative activity

In vitro antiproliferative activity was evaluated using the standard MTT assay. The compounds were dissolved in DMF [63], and each solution was diluted with the culture media (final DMF content was 0.1 %). Cisplatin was used as a positive control. The assay was conducted on human ovarian carcinoma (A2780), cisplatin-resistant ovarian carcinoma (A2780R), prostate adenocarcinoma (PC3), lung adenocarcinoma (A549), breast adenocarcinoma (MCF-7), bone osteosarcoma (HOS), and colorectal (HT-29) cancer cell lines, as well as on the normal human fetal fibroblasts cell line (MRC-5). All cell lines were obtained from the same commercial source (the American Type Culture Collection, ATCC) and maintained according to the producer's instructions. The half-maximal inhibitory concentrations (IC_{50}) were calculated from dose-response curves by means of the GraphPad Prism 6 software (GraphPad Software, San Diego, USA).

4.6.2. Cell culture for mechanistic studies

The human ovarian cancer cell line A2780 (Sigma, 93112519-1VL) was used for additional experiments to investigate the cellular effects of selected diiron complexes. In all experiments, cisplatin (15 μM) and 0.1 % DMF were used as positive and negative controls, respectively. Cells were cultured at 37 °C in a 5 % CO_2 atmosphere in complete RPMI-1640 medium (Merck, USA) supplemented with (final concentrations): L-glutamine (2 mM), fetal bovine serum (FBS, 10 %), penicillin (5 U/mL), and streptomycin (50 μg/mL).

4.6.3. Iron cellular uptake

A2780 cells (10^6) were incubated with half-cytotoxic concentrations of selected diiron complexes for a variable time (2, 6, 12, 24, 48 and 72 h). Following the incubation, adherent cells were detached by trypsinization, washed twice with 0.1 M PBS, and concentrated by centrifugation. Supernatants were discarded, and the resulting cell pellets were digested with 500 μL of ultrapure 65 % nitric acid (at laboratory temperature, overnight). Afterwards, solutions were diluted with 4.5 mL of ultrapure water for trace analysis, and the iron (Fe) content in samples was determined by ICP-MS (ICP-MS spectrometer 7700x, Agilent) using external calibration. The obtained values were corrected for adsorption effects.

4.6.4. Cell cycle

Cell cycle analysis was conducted using the BD Cycletest™ Plus DNA kit (Becton Dickinson, USA). Briefly, 10^4 cells were seeded in a 96-well plate and treated the following day with diiron complexes for 24 h. After treatment, the supernatant was removed, and cells were washed once with warm PBS (0.1 M, pH 7.4). The kit solutions (A, B and C) were then added following the manufacturer's protocol. The samples were analyzed using a BD FACSVerse flow cytometer (Becton Dickinson, USA), with at least 5 x 10^3 events recorded per sample. Measurements were performed in duplicates.

4.6.5. Apoptosis

The potential of selected complexes to induce apoptosis was assessed using two different assays: the Annexin V-FITC apoptosis detection kit (Enzo Life Sciences, USA) and the CellEvent™ Caspase-3/7 Green Flow Cytometry Assay Kit (Thermo Fisher Scientific, USA) to evaluate caspase induction. The apoptosis detection kit was used following the manufacturer's protocol, while only the CellEvent™ Caspase-3/7 Green Detection Reagent was specifically employed for Caspase-3/7 activity.

Briefly, 5 x 10^4 A2780 cells were seeded in a 24-well plate and incubated the following day with diiron complexes for 24 h. After treatment, the supernatant was collected, and the cells were washed with warm PBS (0.1 M, pH 7.4). Cells were then detached with trypsin (0.25 % in ethylenediaminetetraacetic acid-EDTA, Merck), resuspended in 500 μL of culture medium, and divided into separate Eppendorf tubes for apoptosis and Caspase-3/7 detection. Each batch was stained with the appropriate dyes and incubated according to the protocols (10 min in the dark at room temperature for Annexin V-FITC/PI and 30 min in the incubator at 37 °C for the CellEvent™ Caspase-3/7 Green Detection Reagent). Samples were analyzed using a BD FACSVerse flow cytometer (Becton Dickinson, USA), with duplicates per each experiment and at least 5 x 10^3 events recorded per sample. Cisplatin was used as the positive control for apoptosis, while heat-damaged cells (10 min at 60 °C) served as positive control for caspase activation.

4.6.6. Autophagy

To assess the autophagy induction by selected complexes in A2780 cells, the CYTO-ID® Autophagy Detection Kit 2.0 (Enzo Life Sciences, USA) was utilized. Cells were seeded in a 24-well plate (5 x 10^3 cells/well), and the following day cells were treated with the selected diiron complex for 24 h. After treatment, the supernatant was collected, and the cells were washed with warm PBS, detached with trypsin, and resuspended in a warm cell culture medium. The samples were then stained with the diluted CYTO-ID® Green stain solution according to the manufacturer's protocol and incubated in the dark for 30 min at room temperature. Autophagy was measured using a BD FACSVerse flow cytometer (Becton Dickinson, USA), with at least 5 x 10^3 events recorded in duplicates for each sample. A mixture of chloroquine (10 μM) and rapamycin (0.5 μM) for 24 h was used as a positive control.

4.6.7. Mitochondrial membrane potential

The MITO-ID® Membrane Potential Detection Kit (Enzo Life Sciences, USA) was used to evaluate the effect of selected complexes on the mitochondrial membrane potential of A2780 cells. Briefly, cells were seeded in a 24-well plate (5 x 10^4 cells/well). The following day, cells were treated with half-maximal inhibitory concentrations of diiron complexes and incubated for 24 h. After incubation, the supernatant was collected, and cells were washed with PBS, detached with trypsin, and resuspended in cell culture medium. The samples were then incubated with the MITO-ID® Membrane Potential Detection Reagent for 15 min at room temperature, following the manufacturer's protocol. Mitochondrial membrane potential was assessed using a BD FACSVerse flow cytometer (Becton Dickinson, USA), with at least 5 x 10^3 events recorded in duplicates for each sample. A 2 μM carbonyl cyanide-3-chlorophenylhydrazone (CCCP, 30 min incubation) was used as a positive control.

4.6.8. Oxidative stress

To assess oxidative stress in A2780 cells treated with selected complexes, the ROS-ID® Total ROS/Superoxide Detection Kit (Enzo Life Sciences, USA) was employed. Cells were seeded in a 96-well plate (104 cells/well) and exposed to diiron complexes at their half-maximal inhibitory concentrations (as determined by the MTT test), for 24 h. After incubation, the supernatants were removed, and cells were washed with 1X wash buffer. The cells were then stained with ROS/Superoxide Detection Solution for 60 min at 37 °C in the dark, following the manufacturer's instructions. Fluorescence (Ex. 488 nm/Em 520 nm for Total ROS and Ex. 550 nm/Em 610 nm for Superoxide) was measured in triplicate using an Infinite M200Pro microplate reader (Tecan, Switzerland). Pyocyanin (500 μM), a known oxidative stress inducer, was used as a positive control with a 30 min incubation period.

4.6.9. Statistical analysis

Three independent experiments were conducted for both the flow cytometry and oxidative stress analysis. The results are expressed as the mean ± standard deviation (SD). One-way ANOVA with Dunnett's post

hoc test was applied, and statistical significance was denoted as follows: *p ≤ 0.05, **p ≤ 0.01, ***p ≤ 0.001.

Declaration of competing interest

The authors declare no conflicts of interest.

Acknowledgements

We gratefully thank the University of Pisa (Fondi di Ateneo 2022) and the Palacký University in Olomouc for financial support. T.M. acknowledges the financial support by the REFRESH – Research Excellence For Region Sustainability and High-tech Industries project CZ.10.03.01/00/22_003/0000048.

Appendix A. Supplementary data

Supplementary data to this article can be found online at https://doi.org/10.1016/j.cbi.2024.111318.

Data availability

Data will be made available on request.

References

[1] E.J. Anthony, E.M. Bolitho, H.E. Bridgewater, O.W.L. Carter, J.M. Donnelly, C. Imberti, E.C. Lant, F. Lermyte, R.J. Needham, M. Palau, P.J. Sadler, H. Shi, F.-X. Wang, W.-Y. Zhang, Z. Zhang, Metallodrugs are unique: opportunities and challenges of discovery and development, Chem. Sci. 11 (2020) 12888–12917.
[2] M. Marloye, G. Berger, M. Gelbcke, A survey of the mechanisms of action of anticancer transition metal complexes, Future Med. Chem. 8 (2016) 2263–2286.
[3] E. Boros, P.J. Dyson, G. Gasser, Classification of metal-based drugs according to their mechanisms of action, Chem 6 (2020) 41–60.
[4] K.L. Haas, K.J. Franz, Application of metal coordination chemistry to explore and manipulate cell biology, Chem. Rev. 109 (2009) 4921–4960.
[5] S. Ghosh, Cisplatin: the first metal based anticancer drug, Bioorg. Chem. 88 (2019) 102925.
[6] S. Dilruba, G.V. Kalayda, Platinum-based drugs: past, present and future, Cancer Chemother. Pharmacol. 77 (2016) 1103–1124.
[7] R.C. Todd, S.J. Lippard, Inhibition of transcription by platinum antitumor compounds, Metallomics 1 (2009) 280–291.
[8] R. Oun, Y.E. Moussa, N.J. Wheate, The side effects of platinum-based chemotherapy drugs: a review for chemists, Dalton Trans. 47 (2018) 6645–6653.
[9] L. Qi, Q. Luo, Y. Zhang, F. Jia, Y. Zhao, F. Wang, Advances in toxicological Research of the anticancer drug cisplatin, Chem. Res. Toxicol. 32 (2019) 1469–1486.
[10] K. Peng, B.-B. Liang, W. Liu, Z.-W. Mao, What blocks more anticancer platinum complexes from experiment to clinic: major problems and potential strategies from drug design perspectives, Coord. Chem. Rev. 449 (2021) 214210.
[11] B.S. Murray, P.J. Dyson, Recent progress in the development of organometallics for the treatment of cancer, Curr. Opin. Chem. Biol. 56 (2020) 28–34.
[12] M. Mora, M.C. Gimeno, R. Visbal, Recent advances in gold–NHC complexes with biological properties, Chem. Soc. Rev. 48 (2019) 447–462.
[13] Y. Ching Ong, G. Gasser, Organometallic compounds in drug discovery: past, present and future, Drug Discov. Today 37 (2020) 117–124.
[14] C. Santini, M. Pellei, V. Gandin, M. Porchia, F. Tisato, C. Marzano, Advances in copper complexes as anticancer agents, Chem. Rev. 114 (2014) 815–862.
[15] C. Imberti, P.J. Sadler, 150 years of the periodic table: new medicines and diagnostic Agents, Adv. Inorg. Chem. 75 (2020) 3–56. Elsevier.
[16] A. Pilon, A.R. Brás, L. Côrte-Real, F. Avecilla, P.J. Costa, A. Preto, M.H. Garcia, A. Valente, A new family of iron(II)-Cyclopentadienyl compounds shows strong activity against colorectal and triple negative breast cancer cells, Molecules 25 (2020) 1592.
[17] A. Valente, T.S. Morais, R.G. Teixeira, C.P. Matos, A.I. Tomaz, M.H. Garcia, Ruthenium and iron metallodrugs: new inorganic and organometallic complexes as prospective anticancer agents, Synthetic Inorganic Chemistry, chapter 6 (2021) 223–276. Elsevier.
[18] S.S. Braga, A.M.S. Silva, A new age for iron: antitumoral ferrocenes, Organometallics 32 (2013) 5626–5639.
[19] M. Patra, G. Gasser, The medicinal chemistry of ferrocene and its derivatives, Nat. Chem. Rev 1 (2017), https://doi.org/10.1038/s41570-017-0066.
[20] B. Sharma, V. Kumar, Has ferrocene really delivered its role in accentuating the bioactivity of organic scaffolds? J. Med. Chem. 64 (2021) 16865–16921.
[21] A.N. Rodionov, K. Ya Zherebker, L.V. Snegur, A.A. Korlyukov, D.E. Arhipov, A. S. Peregudov, M.M. Ilyin, M.M. Ilyin Jr., O.M. Nikitin, N.B. Morozova, A. A. Simenel, Synthesis, structure and enantiomeric resolution of ferrocenylalkyl mercaptoazoles. Antitumor activity in vivo, J. Organomet. Chem. 783 (2015) 83–91.
[22] Q. Cheng, T. Zhou, Q. Xia, X. Lu, H. Xu, M. Hu, S. Jing, Design of ferrocenylseleno-dopamine derivatives to optimize the Fenton-like reaction efficiency and antitumor efficacy, RSC Adv. 11 (2021) 25477–25483.
[23] L.V. Snegur, A.N. Rodionov, L.A. Ostrovskaya, M.M. Ilyin, A.A. Simenel, Ferrocene-modified imidazoles: one-pot oxalyl chloride-assisted synthesis, HPLC enantiomeric resolution, and in vivo antitumor effects, Appl. Organomet. Chem. (2022) e6681, https://doi.org/10.1002/aoc.6681.
[24] O.A. Lenis-Rojas, S. Cordeiro, M. Horta-Meireles, J.A. Araujo Fernández, S. Fernández Vila, J.A. Rubiolo, P. Cabezas-Sainz, L. Sanchez, A.R. Fernandes, B. Royo, N-heterocyclic carbene iron complexes as anticancer agents: in vitro and in vivo biological studies, Molecules 26 (2021) 5535.
[25] L.V. Snegur, M.V. Lyapunova, D.D. Verina, V.V. Kachala, A.A. Korlyukov, M. M. Ilyin Jr., V.A. Davankov, L.A. Ostrovskaya, N.V. Bluchterova, M.M. Fomina, V. S. Malkov, K.V. Nevskaya, A.G. Pershina, A.A. Simenel, Nitro-imidazoles in ferrocenyl alkylation reaction. Synthesis, enantiomeric resolution and in vitro and in vivo bioeffects, J. Organomet. Chem. 871 (2018) 10–20.
[26] S.-Z. Ren, Z.-C. Wang, D. Zhu, X.-H. Zhu, F.-Q. Shen, S.-Y. Wu, J.-J. Chen, C. Xu, H.-L. Zhu, Design, synthesis and biological evaluation of novel ferrocene-pyrazole derivatives containing nitric oxide donors as COX-2 inhibitors for cancer therapy, Eur. J. Med. Chem. 157 (2018) 909–924.
[27] S. Daum, V.F. Chekun, I.N. Todor, N.Y. Lukianova, Y. Lukianova, Y.V. Shvets, L. Sellner, K. Putzker, J. Lewis, T. Zenz, I.A.M. de Graaf, G.M.M. Groothuis, A. Gasini, O. Zozulia, F. Hampel, A. Mokhir, Improved synthesis of N-benzyl-laminoferrocene-based prodrugs and evaluation of their toxicity and antileukemic activity, J. Med. Chem. 58 (2015) 2015–2024.
[28] V. Ritleng, M.J. Chetcuti, Hydrocarbyl ligand transformations on heterobimetallic complexes, Chem. Rev. 107 (2007) 797–858.
[29] R. Mazzoni, M. Salmi V. Zanotti, C-C bond formation in diiron complexes, Chem. Eur J. 18 (2012) 10174–10194.
[30] F. Marchetti, F. Constructing, Organometallic architectures from aminoalkylidyne diiron complexes, Eur. J. Inorg. Chem. (2018) 3987–4003.
[31] J. Chen, R. Wang, Remarkable reactions of cationic carbyne complexes of manganese, rhenium, and diiron with carbonylmetal anions, Coord. Chem. Rev. 231 (2002) 109–149.
[32] G. Agonigi, M. Bortoluzzi, F. Marchetti, G. Pampaloni, S. Zacchini, V. Zanotti, Regioselective nucleophilic additions to diiron carbonyl complexes containing a bridging aminocarbyne ligand: a synthetic, crystallographic and DFT study, Eur. J. Inorg. Chem. (2018) 960–971.
[33] L. Biancalana, F. Marchetti, Aminocarbyne ligands in organometallic chemistry, Coord. Chem. Rev. 449 (2021) 214203.
[34] L. Biancalana, M. De Franco, G. Ciancaleoni, S. Zacchini, G. Pampaloni, V. Gandin, F. Marchetti, Easily available, amphiphilic diiron cyclopentadienyl complexes exhibit in vitro anticancer activity in 2D and 3D human cancer cells through redox modulation triggered by CO release, Chem. Eur J. 27 (2021) 10169–10185.
[35] H. Ghareeb, N. Metanis, The thioredoxin system: a promising target for cancer drug development, Chem. Eur J. 26 (2020) 10175–10184.
[36] M. Bian, R. Fan, S. Zhao, W. Liu, Targeting the thioredoxin system as a strategy for cancer therapy, J. Med. Chem. 62 (2019) 7309–7321.
[37] I. Ojima, O. Duclos, M. Zucco, M.-C. Bissery, C. Combeau, P. Vrignaud, J.F. Riou, F. Lavelle, Synthesis and structure-activity relationships of new antitumor taxoids. Effects of cyclohexyl substitution at the C-3' and/or C-2 of taxotere (docetaxel), J. Med. Chem. 37 (1994) 2602–2608.
[38] V.R. Akhmetova, N.S. Akhmadiev, M.F. Abdullin, L.U. Dzhemileva, V.A. Dyakonov, Synthesis of new N,N-Pd(Pt) complexes based on sulfanyl pyrazoles, and investigation of their in vitro anticancer activity, RSC Adv. 10 (2020) 15116–15123.
[39] E. Zanda, N. Busto, L. Biancalana, S. Zacchini, T. Biver, B. Garcia, F. Marchetti, Anticancer and antibacterial potential of robust Ruthenium(II) arene complexes regulated by choice of α-diimine and halide ligands, Chem. Biol. Interact. 344 (2021) 109522.
[40] S. Benetti, M. Dalla Pozza, L. Biancalana, S. Zacchini, G. Gasser, F. Marchetti, The beneficial effect of cyclohexyl substituent on the in vitro anticancer activity of diiron vinyliminium complexes, Dalton Trans. 52 (2023) 5724–5741.
[41] M. De Franco, L. Biancalana, C. Zappelli, S. Zacchini, V. Gandin, F. Marchetti, 1,3,5-Triaza-7-phosphaadamantane and cyclohexyl groups impart to di-iron(I) complex aqueous solubility and stability, and prominent anticancer activity in cellular and animal models, J. Med. Chem. 67 (2024) 11138–11151, https://doi.org/10.1021/acs.jmedchem.4c00641.
[42] E. Mihajlović, L. Biancalana, S. Jelača, L. Chiaverini, B. Dojčinović, D. Dunđerović, S. Zacchini, S. Mijatović, D. Maksimović-Ivanić, F. Marchetti, FETPY: a diiron(I) Thio−Carbyne complex with prominent anticancer activity in vitro and in vivo, J. Med. Chem. 67 (2024) 7553–7568.
[43] P. Štarha, Z. Trávníček, Non-platinum complexes containing releasable biologically active ligands, Coord. Chem. Rev. 395 (2019) 130–145.
[44] W.D.J. Tremlett, D.M. Goodman, T.R. Steel, S. Kumar, A. Wieczorek-Błauz, F. P. Walsh, M.P. Sullivan, M. Hanif, C.G. Hartinger, Design concepts of half-sandwich organoruthenium anticancer agents based on bidentate bioactive ligands, Coord. Chem. Rev. 445 (2021) 213950.
[45] E. Bortolamiol, F. Visentin, T. Scattolin, Recent advances in bioconjugated transition metal complexes for cancer therapy, Appl. Sci. 13 (2023) 5561, https://doi.org/10.3390/app13095561.
[46] P. Chellan, P.J. Sadler, Enhancing the activity of drugs by conjugation to organometallic fragments, Chem. Eur J. 26 (2020) 8676–8688.

[47] M. Yang, U. Bierbach, Metal-containing pharmacophores in molecularly targeted anticancer therapies and diagnostics, Eur. J. Inorg. Chem. (2017) 1561–1572.
[48] P. Das, M.D. Delost, M.H. Qureshi, D.T. Smith, J.T. Njardarson, A survey of the structures of US FDA approved combination drugs, J. Med. Chem. 62 (2019) 4265–4311.
[49] S. Prachayasittikul, R. Pingaew, A. Worachartcheewan, N. Sinthupoom, V. Prachayasittikul, S. Ruchirawat, V. Prachayasittikul, Roles of pyridine and pyrimidine derivatives as privileged scaffolds in anticancer agents, Mini-Rev. Med. Chem. 17 (2017) 869–901.
[50] C.M. Clavel, E. Paunescu, P. Nowak-Sliwinska, A.W. Griffoen, R. Scopelliti, P. J. Dyson, Modulating the anticancer activity of ruthenium(II) – arene complexes, J. Med. Chem. 58 (2015) 3356–3365.
[51] Z. Liu, I. Romero-Canelón, A. Habtemariam, G.J. Clarkson, P.J. Sadler, Potent half-sandwich iridium(III) anticancer complexes containing C∧N-chelated and pyridine ligands, Organometallics 33 (2014) 5324–5333.
[52] C. Icsel, V.T. Yilmaz, M. Aygun, M. Erkisa, E. Ulukaya, Novel 5-fluorouracil complexes of Zn(ii) with pyridine-based ligands as potential anticancer agents, Dalton Trans. 51 (2022) 5208–5217.
[53] G. Zhao, H. Lin, Metal complexes with aromatic N-containing ligands as potential agents in cancer treatment, Curr. Med. Chem. Anti Cancer Agents 5 (2005) 137–147.
[54] T.R. Steel, F. Walsh, A. Wieczorek-Błauz, M. Hanif, C.G. Hartinger, Monodentately-coordinated bioactive moieties in multimodal half-sandwich organoruthenium anticancer agents, Coord. Chem. Rev. 439 (2021) 213890 and references therein.
[55] A. Gobbo, S.A.P. Pereira, L. Biancalana, S. Zacchini, M.L.M.F.S. Saraiva, P.J. Dyson, F. Marchetti, Anticancer ruthenium(II) tris(pyrazolyl)methane complexes with bioactive Co-ligands, Dalton Trans. 51 (44) (2022) 17050, https://doi.org/10.1039/D2DT03009H.
[56] G. Bresciani, L. Biancalana, G. Pampaloni, S. Zacchini, G. Ciancaleoni, F. Marchetti, A comprehensive analysis of the metal–nitrile bonding in an organo-diiron system, Molecules 26 (2021) 7088, https://doi.org/10.3390/molecules26237088.
[57] T.-Y. Luh, Trimethylamine N-Oxide-A versatile reagent for organometallic chemistry, Coord. Chem. Rev. 60 (1984) 255–276.
[58] C. Saviozzi, S. Stocchetti, G. Bresciani, L. Biancalana, G. Pampaloni, F. Marchetti, Adding diversity to diiron aminocarbyne complexes with amine ligands, INORGA 11 (2023) 91, https://doi.org/10.3390/inorganics11030091.
[59] L. Busetto, F. Marchetti, S. Zacchini, V. Zanotti, E. Zoli, Diiron-aminocarbyne complexes with amine or imine ligands: C–N coupling between imine and aminocarbyne ligands promoted by tolylacetylide addition to $[Fe_2\{\mu\text{-}CN(Me)R\}(\mu\text{-}CO)(CO)(NH{=}CPh_2)(Cp)_2][SO_3CF_3]$, J. Organomet. Chem. 690 (2005) 348–357.
[60] A.S. Goldman, K. Krogh-Jespersen, Why do cationic carbon monoxide complexes have high C-O stretching force constants and short C-O bonds? Electrostatic effects, not σ-bonding, J. Am. Chem. Soc. 118 (1996) 12159–12166.
[61] J. VelaJeremy, M. Smith, Y. Yu, N.A. Ketterer, C.J. Flaschenriem, R.J. Lachicotte, P.L. Holland, Synthesis and reactivity of low-coordinate iron(II) fluoride complexes and their use in the catalytic hydrodefluorination of fluorocarbons, J. Am. Chem. Soc. 127 (2005) 7857–7870.
[62] The estimated water solubility of cisplatin is 8.4 mM, S. Dasari, P.B. Tchounwou, Cisplatin in cancer therapy: molecular mechanisms of action, Eur. J. Pharmacol. 740 (2014) 364–378.
[63] An organic co-solvent was required to prepare solutions suitable for ^{1}H NMR and cytotoxicity experiments, respectively. DMSO-d_6 was excluded due to its coordinative ability towards diiron(I) aminocarbyne complexes [64]. Among non-coordinating, polar solvents, CD_3OD Was Selected for ^{1}H NMR Analyses Based on its Relatively Low Cost, while DMF Was Used for Cytotoxicity Testing Based on to Literature Recommendations [65].
[64] G. Agonigi, L. Biancalana, M.G. Lupo, M. Montopoli, N. Ferri, S. Zacchini, F. Binacchi, T. Biver, B. Campanella, G. Pampaloni, V. Zanotti, F. Marchetti, Exploring the anticancer potential of diiron bis-cyclopentadienyl complexes with bridging hydrocarbyl ligands: behavior in aqueous media and in vitro cytotoxicity, Organometallics 39 (2020) 645–657.
[65] H. Huang, N. Humbert, V. Bizet, M. Patra, H. Chao, C. Mazet, G. Gasser, Influence of the dissolution solvent on the cytotoxicity of octahedral cationic Ir(III) hydride complexes, J. Organomet. Chem. 839 (2017) 15–18.
[66] Y. He, Q. Zhu, M. Chen, Q. Huang, W. Wang, Q. Li, Y. Huang, W. Di, The changing 50% inhibitory concentration (IC_{50}) of cisplatin: a pilot study on the artifacts of the MTT assay and the precise measurement of density-dependent chemoresistance in ovarian cancer, Oncotarget 7 (2016) 70803–70821.
[67] F. Ricci, V. Berardi, G. Risuleo, Differential cytotoxicity of MEX: a component of neem oil whose action is exerted at the cell membrane level, Molecules 14 (2009) 122–132.
[68] A. Mameri, L. Bournine, L. Mouni, S. Bensalem, M. Iguer-Ouada, Oxidative stress as an underlying mechanism of anticancer drugs cytotoxicity on human red blood cells' membrane, Toxicol. Vitro 72 (2021) 105106.
[69] J. Wang, G. Sheng, Role of autophagy in cisplatin resistance in ovarian cancer cells, J. Biol. Chem. 289 (2014) 17163–17173.
[70] D. Arora, S. Hall, S. Anoopkumar-Dukie, R. Morrison, A. McFarland, A.V. Perkins, A.K. Davey, G.D. Grant, Pyocyanin induces systemic oxidative stress, inflammation and behavioral changes in vivo, Toxicol. Mech. Methods 28 (2018) 410–414.
[71] J.P. Kamat, T.P.A. Devasagayam, Nicotinamide (vitamin B3) as an effective antioxidant against oxidative damage in rat brain mitochondria, Commun. Free Rad. Res. 4 (1999) 179–184.
[72] A.J. Kowaltowski, A.E. Vercesi, Mitochondrial damage induced by conditions of oxidative stress, Free Rad, Biol. Med. 26 (1999) 463–471.
[73] M. Ott, V. Gogvadze, S. Orrenius, B. Zhivotovsky, Mitochondria, oxidative stress and cell death, Apoptosis 12 (2007) 913–922.
[74] Menges, F. "Spectragryph - optical spectroscopy software", Version 1.2.5, @ 2016-2017, http://www.effemm2.de/spectragryph.
[75] G.R. Fulmer, A.J.M. Miller, N.H. Sherden, H.E. Gottlieb, A. Nudelman, B.M. Stoltz, J.E. Bercaw, K.I. Goldberg, NMR chemical shifts of trace impurities: common laboratory solvents, organics, and gases in deuterated solvents relevant to the organometallic chemist, Organometallics 29 (2010) 2176–2179.
[76] G.M. Sheldrick, Crystal structure refinement with SHELXL, Acta Crystallogr. C 71 (2015) 3–8.
[77] OECD guidelines for testing of chemicals, OECD 107 (1995). Paris.
[78] J.C. Dearden, G.M. Bresnen, The measurement of partition coefficients, Quant. Struct.-Act. Relat. 7 (1988) 133–144.
[79] Calculated by the Formula pD = pH* + 0.4, where pH* Is the Value Measured for H2O-Calibrated pH-Meter; (A) C. C. Westcott, pH Measurements; Academic Press, New York, 1978;
(b) A.K. Covington, M. Paabo, R.A. Robinson, R.G. Bates, Anal. Chem. 40 (1968) 700–706.